POLITECNICO
MILANO 1863

SCUOLA DI INGEGNERIA INDUSTRIALE
E DELL'INFORMAZIONE

Continuum approach for fragmentation event modelling and breakup severity assessment in Low Earth Orbit

Tesi di Laurea Magistrale in
Space Engineering - Ingegneria Spaziale

Author: **Francesca Ottoboni**

Student ID: 991348
Advisor: Prof. Camilla Colombo
Co-advisors: Lorenzo Giudici, Martina Rusconi
Academic Year: 2022-23

This content is original, written by the Author, Francesca Ottoboni. All the non-originals information, taken from previous works, are specified and recorded in the Bibliography.

When referring to this work, full bibliographic details must be given, i.e.
Francesca Ottoboni, "Continuum approach for fragmentation event modelling and breakup severity assessment in Low Earth Orbit". 2023, Politecnico di Milano, Faculty of Industrial Engineering, Department of Aerospace Science and Technologies, Master in Space Engineering, Supervisor: Camilla Colombo, Co-supervisors: Lorenzo Giudici, Martina Rusconi.

Printed in Italy

Abstract

The sustainability of the space environment around the Earth is becoming an increasingly important research topic in the space sector. Past space missions have left a large number of inoperative objects in orbit, which contribute to the space debris population and its exponential growth, posing an increasing risk to operational satellites. Throughout the years, international efforts have focused on the largest bodies in the debris population, constantly tracking objects larger than 10 cm and studying their evolution. However, in recent years studies have demonstrated the importance of tracking smaller objects as well, which pose a significant hazard to other spacecraft. To define mitigation guidelines, it is necessary to take into account the risk posed by the small, so-called untrackable objects, allowing to picture the actual health of the space environment and its evolution.
The traditional semi-deterministic methods used to model the debris population require the propagation of the trajectories of sample fragments in debris clouds, which limits the range of analyses that can be performed. In this thesis, a continuum approach is used to characterise debris clouds in Low Earth Orbit. Fragmentation events are modelled through the NASA Standard Breakup Model, then they are studied as a whole, modelled as a fluid whose spatial density varies in time under the effect of drag. Under some simplifying assumptions, an analytical expression for the cloud density evolution in time is determined from the continuity equation. Different classifications of the fragments according to their area-to-mass ratio are analysed to obtain the most accurate results. The spatial density evolution is then used to characterise the collision probability between the fragments generated by a fragmentation event and given target spacecraft, using an analogy with gas kinetics theory. This model is applied to the assessment of the severity of breakups occurring at various altitudes and inclinations in Low Earth Orbit with respect to a set of reference targets given at various epochs. A novelty is introduced in the computation of the maps to account for the lifetime of the debris clouds, leading to a more accurate representation of breakups at low altitudes. The resulting severity maps allow to understand the effect of the increase of operational satellites in orbit and of constellations as well as the most dangerous regions in Low Earth Orbit for spacecraft. Once they have been obtained, the maps are useful to determine a more sustainable access to space as they

allow to assess the impact of future missions on the already crowded debris environment and they can support the identification of the most meaningful targets for Active Debris Removal. This thesis was part of the GREEN SPECIES project: "Robust control of the space debris population to define optimal policies and an economic revenue model for the sustainable development of space activities" (Grant agreement No. 101089265). This project is European Research Council (ERC) funded project under the European Europe research.

Keywords: space debris, Low Earth Orbit, continuum approach, fragmentation events, collision probability, debris index

Sommario

La sostenibilità dell'ambiente spaziale attorno alla terra sta diventando un argomento di ricerca sempre più importante nel settore spaziale. Le missioni spaziali passate hanno lasciato un grande numero di oggetti inattivi in orbita, i quali contribuiscono alla popolazione di detriti spaziali e alla sua crescita esponenziale, rappresentando un rischio crescente per i satelliti operativi. Negli anni, gli sforzi internazionali si sono concentrati sugli oggetti più grandi della popolazione di detriti, monitorando costantemente gli oggetti più grandi di 10 cm e studiando la loro evoluzione. Tuttavia, in anni più recenti studi hanno dimostrato anche l'importanza del monitoraggio degli oggetti più piccoli, che rappresentano un pericolo concreto per gli altri satelliti. Per definire le linee guida è necessario considerare il rischio rappresentato dai piccoli oggetti, definiti non tracciabili, permettendo così di rappresentare l'effettiva salute dell'ambiente spaziale e la sua evoluzione.
I tradizionali metodi semi-deterministici per modellare la popolazione di detriti richiedono la propagazione delle traiettorie di frammenti rappresentativi nelle nuvole di detriti, limitando la gamma di analisi che possono essere eseguite. In questa tesi, un approccio continuo è utilizzato per caratterizzare le nuvole di detriti in Orbita Terrestre Bassa. Le frammentazioni sono modellate tramite il modello standard di frammentazione della NASA, poi vengono studiate per intero, modellandole come un fluido la cui densità spaziale varia nel tempo per effetto della resistenza atmosferica. Con alcune ipotesi semplificative, è ricavata dall'equazione di continuità un'espressione analitica per l'evoluzione nel tempo della densità spaziale della nuvola. Sono analizzate diverse classificazioni dei frammenti riguardanti il loro rapporto area su massa, per ottenere risultati più accurati possibile. L'evoluzione della densità spaziale viene poi utilizzata per caratterizzare la probabilità di collisione tra i frammenti generati da una frammentazione e dei satelliti target dati, utilizzando un'analogia con la teoria cinetica dei gas. Il modello è applicato per valutare la gravità di frammentazioni che avvengono a varie altitudini e inclinazioni in Orbita Terrestre Bassa rispetto a un set di target di riferimento dato a varie epoche. Per il calcolo delle mappe, è introdotta una novità per considerare la durata della vita delle nuvole di detriti, portando ad una rappresentazione più accurata delle frammentazioni a basse altitudini. Le mappe di gravità risultanti permettono di capire l'effetto dell'aumento di

satelliti operativi in orbita e di costellazioni, nonchè le regioni più pericolose in Orbita Terrestre Bassa per i satelliti. Una volta ottenute, le mappe sono utili per determinare un accesso più sostenibile allo spazio, dal momento che permettono di valutare l'impatto delle missioni future sull'ambiente già popolato di detriti, inoltre possono supportare l'identificazione dei target più rappresentativi per la rimozione attiva di detriti. Questa tesi fa parte del progetto GREEN SPECIES: "Robust control of the space debris population to define optimal policies and an economic revenue model for the sustainable development of space activities" (Grant agreement No. 101089265). Questo progetto è finanziato dall'European Research Council (ERC) nell'ambito della ricerca European Europe.

Parole chiave: detriti spaziali, orbita terrestre bassa, approccio continuo, eventi di frammentazione, probabilità di collisione, indice di detriti

Contents

Abstract **i**

Sommario **iii**

Contents **v**

1 Introduction **1**

1.1 State of the art . . . 4
1.1.1 Probabilistic approach . . . 5
1.1.2 Semi-deterministic models . . . 10
1.1.3 Sustainability metrics . . . 11
1.2 Aim of the thesis . . . 12
1.3 Contribution . . . 13
1.4 Structure of the thesis . . . 14

2 Continuum formulation for a fragmentation event **15**

2.1 Breakup model . . . 15
2.2 Numerical propagation . . . 17
2.2.1 Initial conditions . . . 18
2.2.2 Cloud evolution and band formation . . . 18
2.2.3 Numerical integration - King-Hele's formulation . . . 20
2.3 Spatial Density Function . . . 23
2.4 Continuum formulation . . . 24
2.5 A/M bins definition . . . 27
2.5.1 Optimal bin definition . . . 28
2.5.2 Optimal bin number . . . 30
2.6 Results . . . 33
2.6.1 Computational comparison . . . 38

3 Collision Probability **41**
3.1 Analogy with gas kinetics 41
3.2 Impact rate and collision velocity estimation 42
3.3 Collision probability results 45

4 Effect maps **49**
4.1 Adopted formulation 49
4.1.1 Lifetime of a debris cloud 52
4.1.2 Scenario 1 - Catastrophic collision 55
4.1.3 Scenario 2 - Non-catastrophic collision 60
4.1.4 Scenario 3 - Explosion 62

5 Conclusions and future developments **65**
5.1 Summary 65
5.2 Limitations and future work 66

Bibliography **69**

A Appendix A **77**

B Appendix B **81**
B.1 General method 81
B.2 Application 82

List of Figures **85**

List of Tables **87**

List of Symbols **90**

Acronyms **93**

Acknowledgements **95**

1 | Introduction

Since the beginning of space activity, more than 15800 satellites have been placed into orbit, out of which only about 8700 are still functional among the 10500 satellites still in orbit [10]. According to the European Space Agency (ESA), the Space Surveillance Networks regularly tracks and catalogues about 35030 debris objects, yet since only objects bigger than 5-10 cm can be tracked, the actual number of debris estimated statistically reaches one million when considering objects larger than 1 cm [53]. For this reason, nowadays the modelling of space debris around the Earth and their evolution are prominent research topics. The largest part of space debris is caused by in-orbit fragmentations [53], mainly generated by explosions of spacecraft and upper stages, and collisions. It is estimated that over the last two decades, 11.2 non deliberate fragmentations have occurred each year, causing a population in the order of 90000 objects larger than 1 cm [53]. The explosions take place mainly as a result of stagnant reservoirs of fuel in the tanks or in the pipes, or other energy sources remaining on board such as batteries, leading to leaking and self-ignition, hence breaking up the satellite in fragments [12]. When studying objects in the space environment, it is important to distinguish between *identified* and *unidentified* objects. As reported by ESA's annual space environment report [53], the latter are the objects which cannot be traced back to the launch event, while the former can be further divided into the following categories:

- Payloads, which include operational satellites.
- Rocket bodies, which include the orbital stages of launch vehicles.
- Mission Related Objects (MRO), which can be related to both payloads and rocket bodies. They are objects released as debris during on-orbit operations and deorbit, which served a specific purpose during missions. Examples of MRO are covers for optical instruments, spring release mechanisms and shrouds.
- Fragmentation debris, generated from collisions between a payload and another object or explosions of payloads and rocket bodies. This category contains the highest number of objects.

- Debris related to anomalous events. They are due to unintentional separations of one or more objects from the satellite, usually at low velocity [26]. These events may result from material deterioration of objects and they generate less debris than breakups.

Moreover, the last decade has witnessed significant changes in space traffic, due to the miniaturisation of space systems and the deployment of large constellations, particularly in Low Earth Orbit (LEO). 2023 ESA's annual space environment report [53] disclosed that in 2022 the launch traffic in all mass and type classes overcome historical rates. The evolution of the number of objects in geocentric orbits can be seen in Figure 1.1.

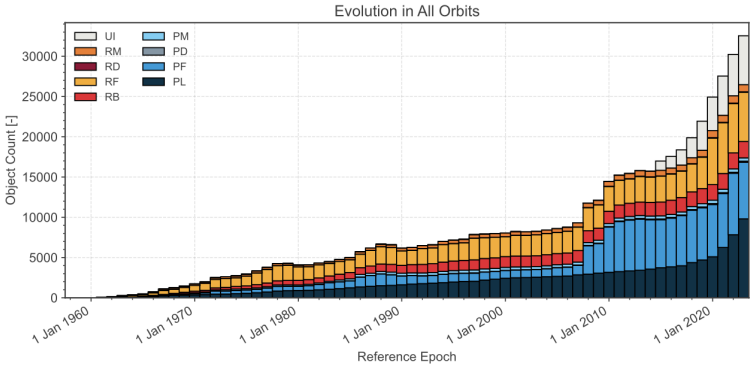

Figure 1.1: Evolution of the number of objects in geocentric orbit [53].

A sudden increase in the number of objects can be seen in Figure 1.1 in correspondence of 2007. This is due to the breakup of the 880 kg weather spacecraft Fengyun-1C on 11 January 2007 as a result of the first successful Chinese anti-satellite weapon test [54]. The altitude of the fragmentation was about 863 km, however the impact of the event was significant in all altitudes between 700 and 1000 km, leading to an increase of 60% in the catalogued object density at the height of the satellite. To this day, the debris cloud generated by the breakup is considered the worst contamination in LEO [26].
Another notable increase in the number of objects is due to the catastrophic collision between the satellites Cosmos 2251 and Iridium 33 on 10 February 2009. Cosmos 2251 was a 900 kg spacecraft, already decommissioned at the time of the breakup, while Iridium 33 was an operational 556 kg spacecraft. This was the first catastrophic collision between two intact satellites. It occurred at an altitude of 789 km, spreading fragments between 200 and 1800 km. It was caused by the lack of accurate information on the location of Cosmos 2251 available to the operators [55].
It is worth to mention a third catastrophic event which has taken place relatively recently. This is the Russian anti-satellite weapon test performed on 15 November 2021 which

destroyed the 1750 kg Cosmos 1408 satellite. The test was carried out at 480 km of altitude leading to the generation of more than 1700 trackable objects and about 60000 fragments under 1 cm scattered between 200 and 1500 km [56]. This event nearly doubled the average flux of the catalogued objects on the International Space Station, posing a threat to the station and to the astronauts inside.

The uncontrolled growth of the debris population is not a newly-discovered issue, as in 1978 Kessler and Cour-Palais [28] had already concluded that if the past growth rate in the catalogued population continued, a distribution of small and dangerous objects would be generated by random collisions, until over a long period of time, the total area of the population would be dominated by the smaller objects. This would cause a continuous increase in the population, becoming exponential [29]. This process of collisional cascading is commonly referred to as *Kessler syndrome* and it allows to understand the need for an accurate picture of the debris environment. Adding to the issue, the numerous small objects present in LEO, which cannot be tracked by radars, cannot be monitored and avoided with collision avoidance manoeuvres in case of conjunction [33]. Shields may be used to protect spacecraft from smaller debris, however up to now they are employed on the International Space Station only. Moreover, they are only effective for fragments smaller than 1 cm [34]. Therefore, it is important to be able to predict the motion of all fragments in orbit and the associated collision risk.

Considering this scenario and the perspective of the Earth's orbital environment as a finite resource, space agencies worldwide have adopted guidelines for mitigation purposes. The Inter-Agency Space Debris Coordination Committee (IADC) is the entity regulating mitigation measures; it is the result of the joint effort of 13 space agencies, including ESA, which aims at standardising the mitigation measures and facilitating international cooperation to achieve a common understanding of the tasks required to face the debris issue [52]. The Post Mission Disposal (PMD) guidelines concern the disposal of satellites in Low Earth Orbit (LEO) and Geostationary Orbit (GEO). For satellites in LEO the recommended action is the limitation of their lifetime in orbit after the end of their mission to 25 years ("25-year rule"). Although this mitigation measure does not provide a specific way to achieve the disposal, there is an order of preference for different techniques. The preferred one consists in placing satellites on orbits which ensure a naturally occurring orbital decay due to drag [52]. For satellites in GEO instead, the recommendation is to exploit graveyard orbits sufficiently above the GEO region. The recommended deorbit altitude is about 300 km above the GEO ring [11]. The guidelines also encompass passivation, which means that all the reservoirs of energy in a rocket body or satellite must be depleted, to avoid the risk of explosions. Even though the guidelines have contributed to

an improvement in the current situation, with an increasing number of compliant satellites, it is estimated that between 40% and 70% of all payload mass is operating in orbits which naturally comply with the measures, while for objects on non-naturally compliant orbits, between 20% and 50% attempt to adhere to the mitigation measures [52]. The target for the success rate of compliance to mitigation guidelines is 90% [53]. Despite an increase in the adoption of these measures, the successful implementation is still too low for a sustainable use of space. As demonstrated by Kessler et al. [29], due to the critical situation, even 100% compliance with PMD guidelines would not prevent the debris environment from growing. This is clearly shown in the more recent extrapolation of the current use of space (Figure 1.2), which indicates that even if launches were halted, the collisions among in-orbit fragments would lead to a growth in the debris population.

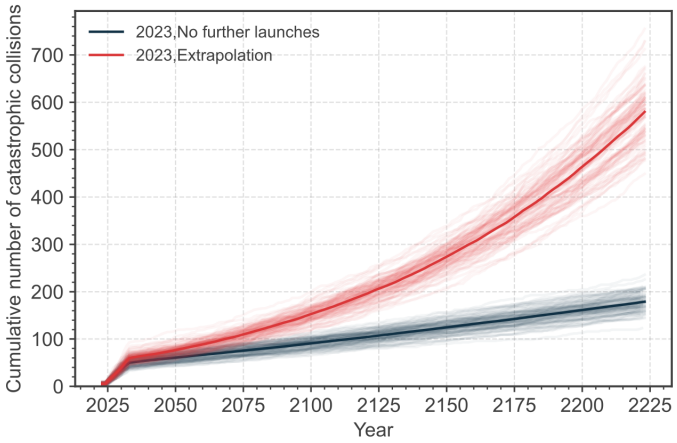

Figure 1.2: Cumulative number of catastrophic collisions in the simulated long-term evolution of the environment [53].

Taking into account all the previous considerations, it is evident that precise models to describe the debris environment and its evolution are necessary to guarantee a responsible and sustainable use of space. This kind of models allows to carry out analyses to ensure the safety for both current and future operational satellites in the space around the Earth.

1.1. State of the art

In order to monitor the debris population and the related risks, many models have been developed throughout the years. In this Chapter, two main approaches are described: the probabilistic models and the semi-deterministic ones. The semi-deterministic models require higher computational power because they follow the individual trajectories of representative sample fragments, hence they have been developed historically later than

the probabilistic ones. The latter deal with the fragmentation cloud as a whole instead. Then, an overview of the main space debris indeces is detailed.

1.1.1. Probabilistic approach

The probabilistic approach stems from the idea of considering the debris fragment cloud as a whole, by treating the debris population as a fluid with continuous properties. This idea was put forth by Heard for the description of the cloud after a breakup [21], then McInnes [46] studied the long-term evolution of the debris density under the effect of perturbations [31]. This method offers a significant reduction in computational time with respect to high-fidelity semi-deterministic approaches, thanks to its statistical formulation, which renders it independent of the number of fragments under consideration.
The method is based on the continuity equation, traditionally used in fluid dynamics. It has been applied to a variety of scenarios in astrodynamics thanks to its generality, such as the evolution of nanosatellites constellations [47] and interplanetary dust [20]. It can also provide the variation in time of the fragment density under perturbations. In this way, the debris cloud is described only through its density n with the continuity equation:

$$\frac{\partial n}{\partial t} + \nabla \cdot (n\mathbf{f}) = \dot{n}^{+} - \dot{n}^{-}, \tag{1.1}$$

where $\nabla \cdot (n\mathbf{f})$ represents the slow/continuous phenomena, e.g. the drag effect, and $\dot{n}^{+} - \dot{n}^{-}$ accounts for the *sources and sinks* of the system, i.e. the fast/discontinuous events, for instance the injection of new fragments due to launches and collisions.
One crucial aspect of the continuum approach is the solution of the continuity equation, which involves a Partial Differential Equation (PDE). Two main approaches can be adopted in order to do this in the context of space debris: reducing the PDE into a set of Ordinary Differential Equations (ODE) with the method of characteristics, or using a temporal and spatial discretisation of the PDE, typically with the finite difference scheme.

Method of characteristics

The application of the method of characteristics to the continuity equation has led to a fully analytical solution, first found by McInnes in [46], where the equation was written as a function of radial distance r and time t only. In order to achieve the closed-form solution, a set of simplifying assumptions has been adopted: an exponential model for atmospheric drag (assumed as the dominant perturbation), quasi-circular orbits, no atmospheric rotation. Starting from the results presented by McInnes [46], the method has

been extended by Letizia et al. [33] from the global debris population to a single fragmentation event for long-term applications, developing the so-called debris Cloud Evolution in Low (Earth) Orbit (CiELO) model. To do this, it is necessary to simulate the generation of fragments due to collisions [31], which is achieved by taking the initial conditions from the NASA Standard Breakup Model [25]. The CiELO method represents an improvement with respect to the original work of McInnes also due to the introduction of a classification of the fragments into bins according to their area-to-mass ratio, on top of the already applied subdivision of fragments into altitude bins. Solving the continuity equation in each area-to-mass ratio bin separately improves the accuracy of the model. This adaptation of the original model allows to include small fragments in the analysis since the state variable of the problem, i.e. the spatial density, is little affected by the number of fragments, therefore no additional computational effort is required. This is an important development as it grants an improvement in the accuracy of estimation of the consequences of a single fragmentation event and of the collision risk associated to it with respect to past models. Despite the advantages of this approach, the monodimensional model developed in CiELO [34] has two main drawbacks [37]:

- It does not account for the Earth's oblateness, as it considers aerodynamic drag to be the main perturbation;
- The method is applicable only at 700 km of altitudes and above, as the analytical solution to the continuity equation relies on the hypothesis of quasi-circular orbits.

To tackle these issues, a multidimensional extension of the method has been developed by Letizia et al. [37], following the approach by Gor'kavyi [20]. Even though the multidimensional approach results in remarkable improvements when compared with the 1D model, the assumptions of quasi-circular orbits and of constant eccentricity must be retained in order to find an analytical solution to the continuity equation.

Following the same approach, a first attempt to apply the continuous technique to the global population of space debris has been carried out by Colombo et al. [5]. By developing the previous model as a function of semi-major axis and eccentricity and under the simplifying assumption of no sources and sinks, the superimposition of effects is employed to model the consequence of a fragmentation onto the background population. Then, the overall population given by the original one and the generated fragments is propagated according to the continuum method.

The previous approaches are based on finding analytical solutions for the continuity equation. The advantage of a fully analytical model is that, once the initial density is known, the cloud density at any time and point in space is known as well, without the need for long-term numerical propagation of the fragment trajectories. On the other hand, the

simplifying assumptions required for the analytical solution limit its applicability [31], hence numerical integration of the characteristics provides a larger flexibility in using more complex dynamics. This approach has been used, for example, to model uncertainties of objects re-entering through the atmosphere in [68]. Nonetheless, the result of the integration of ODE is known only along the characteristics of the system. Therefore, interpolation between the characteristics is necessary to retrieve the solution along the full domain [16].

Finite differences and particle-in-a-box

An alternative to the analytical solution of the continuity equation is the approximation through discretisation. Using the finite differences method, a space discretisation of the continuity equation is obtained within each bin. The set of equations is integrated numerically simultaneously, with a time-step size chosen in order to guarantee numerical stability. This method, coupled with an Euler forward scheme for the time variable, has been implemented by Letizia in [32], in order to overcome the limits of the fully analytical formulation. Specifically, the aim was the extension of the continuum formulation - using the semi-major axis and eccentricity as independent variables - at high and low altitudes, respectively above 1000 km and below 700 km. The results highlight that the analytical approach is accurate enough to represent the debris cloud density at high altitudes, without the need to include Solar Radiation Pressure (SRP) in the model within reasonable altitudes. The finite differences are instead necessary for the applicability of the method at lower altitudes, where the results have outperformed the ones obtained with the analytical solution.

Often, the number of objects in each bin is propagated instead of the density, in the so-called "particles-in-a-box" (PIB) approach. Provided that the bin size is constant, there is a correspondence between this approach and finding the density with the finite differences as the number of objects in a bin is given by the product of the bin density and its volume.

The first instances of the use of the PIB approach in debris modelling can be found in the independent works of Talent [67] and Farinella and Cordelli [13]. They consist in using differential equations, to be numerically integrated, to express the rate of change of the number of objects in orbit, instead of the density. This approach can model collisions, removals, launches and explosions, leading to respectively one first-order differential equation for the whole model in [67] and two paired first-order differential equations in [13]. Further work by Rossi et al. [59] allowed to extend the earlier work by Farinella and Cordelli [13] by introducing altitude shells and logarithmic bins in mass, leading to 150

coupled first-order ODE. Lastly, the model was modified in [60] to use orbital elements instead of altitude shells, employing semi-major axis and eccentricity bins.
More recently, the same kind of approach has been followed by Somma et al. [63–65], developing a multi-species and multi-shell source-sink model for LEO based on differential equations computing the rate of change of the number of orbiting objects. This work also introduces an adaptive feedback controller on Active Debris Removal (ADR) in the model, enabling sensitivity analyses in terms of launch rates and PMD.

Extension of the model - Starling suite

The extension of the continuum approach to higher altitudes was limited by the simplified force models and restricted orbital geometries required by the analytical model. The extension with the finite differences also presents significant obstacles despite the flexibility guaranteed by the method. As pointed out by Frey et al. [16], solutions relying on this approach are able to model the distribution over the full domain, yet they are difficult to extend to more than three dimensions because of restrictions in terms of computational power and memory. These issues have been addressed with the Starling suite [16], which allows to estimate evolving continua subject to non-linear dynamics. Thanks to the Starling suite, it is possible to incorporate accurate force models and modelling of densities in any orbit, while seamlessly increasing or decreasing the dimensionality of the problem and maintaining relatively low computational requirements (compared to semi-deterministic models). The tool is based on the continuum formulation, which is applied right after the fragmentation event since the force models employed in Starling are able to deal with the first phases of the debris cloud evolution as well, contrary to the CiELO method. The first version of Starling numerically propagates the continuity equation along the characteristics using the *PlanODyn* suite [4], then a Gaussian Mixture Model (GMM) is fitted to the characteristics to retrieve the density distribution in the phase space of Keplerian elements and area-to-mass ratio. While Starling potentially extends the continuum approach to any orbital regime, it has some limitations as well. Specifically, its applicability depends on the ability of describing the density of the fragments as sums of Gaussian distributions [19]. Frey et al. [16] pointed out that the method is not able to accommodate forces that lead to resonances on a small subset of the phase space, such as third-body perturbations or solar radiation pressure. These resonances create bifurcations that pose challenges when attempting to model the distribution using a GMM. Further work by Giudici et al. [19] has been aimed at overcoming these issues and developing a method for propagation of fragment clouds truly under any dynamical regime. This was achieved by combining the use of the method of characteristics with a binning approach

over the phase space of Keplerian elements and area-to-mass ratio for the interpolation of characteristics, as it is supposed to be independent from the considered dynamical regime. The main drawback of the binning approach over a multi-dimensional phase space is the required computational effort. This was addressed by using probabilistic models to estimate the distribution of fragments in the phase space, allowing to propagate the debris' cloud only in the regions of the phase space which are more likely to host the ejected fragments over time [19].

Collision probability

One of the many advantages of using the continuum approach is the possibility of quickly evaluating how a debris cloud affects the collision probability for near spacecraft. In 1951, Öpik [72] derived equations which related the probability of collision between two orbiting objects to their orbital elements, however the method was limited by specific assumptions, as one of the objects was always assumed to have zero eccentricity and inclination. Starting from Öpik's equations, Kessler [27] used the concept of spatial density, following the analogy with the kinetic gas theory, and applied it both to the general case of two orbiting objects and to the debris environment [66]. According to the analogy, the average number of collisions between a target and the fragments can be modelled as the collisions among molecules within an inert gas. The collision probability is obtained by modelling the collisions as a Poisson process, under certain hypotheses [58]. Jenkin [23] has pointed out that the method is not valid in the first phases of the cloud evolution, however it holds for the final phase in which the fragments have reached the band configuration and their motion has randomised. Following this procedure, the collision probability computation block has been added to the CiELO method developed by Letizia et al. [36], with some minor adjustments with respect to the previous works. Indeed, assuming the random motion of the fragments from the moment of band formation (hence assuming the argument of perigee, mean anomaly and right ascension of the ascending node randomised), the analytical solution of the average relative velocity between fragments and target is found. For improved accuracy, the collision probability computation has been extended to 2D [35].

A further evolution of the spatial density approach developed by Kessler [27] for collision probability evaluation is the Cube algorithm developed by Liou [43]. Here, the kinetic gas theory is used at microscopic scale to evaluate the collision probability between objects within a cube, taken as a reference volume. The Cube algorithm is able to estimate the long-term collision probabilities using uniform sampling of the system in time with updated objects and their orbital elements at each time step. This algorithm is largely

employed, thanks to its flexibility, which makes it applicable to the fast-changing debris environment, to debris populations in both the physical and orbital elements space [43].

1.1.2. Semi-deterministic models

The semi-deterministic approach for debris modelling is based on the propagation of the orbital elements of individual fragments, as opposed to looking at the debris cloud as a whole. These *debris evolutionary models* follow the long-term evolution of space debris, aiming to model the global debris population instead of single events, by relying on semi-analytical propagators. In order to carry out the simulations, a set of assumptions is required [31]:

- on natural phenomena (atmosphere model, solar flux);
- on future activities (number of launches, compliance with mitigation guidelines, active removal);
- on debris evolution (criteria for collision, number of fragmentation events per year).

The drawback of using simplifying assumptions is the loss of certainty and accuracy that they imply. This is particularly critical as the debris evolutionary models are required to supply precise information for decision making, both for the long and short-term. To overcome the issue, as well as the absence of a comprehensive set of experimental data, the Monte Carlo method is employed: each scenario of debris evolution is run between 10 and 1000 times [31], to get reliable data. However, the Monte Carlo simulations add a significant computational burden, which limits the applicability of these models. Moreover, the debris evolutionary models currently neglect fragments smaller than 10 cm [33] due to the high number of small objects in orbit, considering only the trackable ones. Despite their drawbacks, evolutionary models have been developed by all the major space agencies as well as universities. Some of the available models are described hereafter.
ESA's Debris Environment Long Term Analysis (DELTA) is a three-dimensional, semi-deterministic model, developed by Walker et al. [71], which allows to study the evolution of the debris environment and the collision risks associated to it for Low, Medium and Geosynchronous Earth orbit. In DELTA, the population is described by representative objects, whose trajectories are followed by using a fast analytical orbit propagator accounting for the main perturbations, i.e. atmospheric drag, luni-solar gravitational effects, SRP and geopotential [70]. As opposed to the majority of long-term evolution tools, the collision probability is evaluated through a flux-based technique. DELTA is able to simulate the implementation of multiple mitigation measures as well as active debris removal, allowing the assessment of the efficacy of these measures, while maintaining high-fidelity due to

the use of detailed future traffic models.
The Space Debris Mitigation (SDM) model by Rossi et al. [60] is designed to follow the actual orbit evolution of objects. Its most recent version (4.0) is a full 3D LEO to GEO simulation code, useful for long-term analyses, particularly in the MEO and GEO regions [61]. The population considered in SDM is divided into two categories: historical population and running population, then three orbital propagators are available for their evolution, to be selected according to the different orbital regimes and the accuracy required. The collision probability can then be computed by choosing from two different approaches, namely the analytical approach developed by Öpik [72] or the Cube algorithm [43] developed by Liou [43]. SDM is able to simulate mitigation strategies, concerning constellations as well and active debris removal.
NASA's LEO-to-GEO Environment Debris (LEGEND) is a full-scale, three-dimensional debris evolutionary model [44], able to reproduce the historical debris environment and to make projections on the future one. It covers LEO, MEO and GEO and super-GEO (above 38000 km) and it employs two orbital propagators: PROP3D, to compute the motion of GEO objects and GEO-PROP for the remaining orbital bodies. PROP3D considers as main perturbations atmospheric drag, solar and lunar gravitational perturbations, SRP, the Earth's shadow effects and the Earth's gravity field zonal harmonics, whereas GEO-PROP accounts for atmospheric drag, solar and lunar gravitational perturbations, SRP and the Earth's gravity field zonal and tesseral harmonics perturbations.

1.1.3. Sustainability metrics

The results of the long-term propagation of the debris environment have shown the need for mitigation measures and guidelines. On top of these, space debris indices have been formulated to ensure a more sustainable access to space. They aim to assess the criticality of individual objects with respect to their contribution to the space debris environment [41]. These metrics focus on different aspects of the space debris environment, allowing to understand the most influential parameters on the space debris evolution and the identification of the most dangerous spacecraft, to be potentially removed with active debris removal [38]. Among the proposed metrics, Rossi et al. [62] have formulated the Criticality of Spacecraft Index (CSI), aimed at ranking the criticality of abandoned spacecraft in LEO. The index considers the dependence with respect to the environment in terms of spatial density, the dependence on the lifetime and mass of the objects and on their orbital inclination. The advantage of this metric is that it is easily understandable since the higher the value of the index, the more dangerous the object in terms of effects on the space environment.

Similarly, Anselmo and Pardini [1] have developed a formulation to rank the detrimental effects of upper stages in LEO, although the scheme is applicable to any object in LEO. The ranking index depends on the current flux of orbital debris, the lifetime and the mass of the considered object.
Lewis et al. [42] have proposed another metric, similar to the previous ones for the evaluation of the impact of a candidate spacecraft on the environment through a rating system, yet different since it comprises two stages. The first one is the computation of an index of the health of the environment, evaluated through a set of environmental goals and describing the ability of the environment to support long-term space activities. The second part instead rates a spacecraft for its ability to improve the health of its local region based on its characteristics.
A different approach has been put forth by Letizia et al. [38], who formulated the Environmental Consequences of Orbital Breakups (ECOB) index. In its original formulation, the index assessed the severity of potential breakups occurring at different altitudes and inclinations in LEO. The effect of the breakups is measured by the collision probability for given targets with the debris generated by the breakup in time, evaluating the evolution of debris clouds with the CiELO method. Further work by Letizia et al. [39] has extended the applicability of the index and enhanced it to account for the likelihood of the fragmentations as well, computing their probability starting from the debris population. The computation of the ECOB index extended to any orbital regime has been achieved and incorporated in the Track the Health of the Environment and Missions in Space (THEMIS) tool [6] developed at Politecnico di Milano. In its space debris mode, THEMIS allows the computation of the index given the profile of a mission, the spacecraft and orbital characteristics, and operational aspects. As explained by Muciaccia et al. [51], the index computation in THEMIS is carried out throughout the entire lifetime of the mission, taking into account the Post Mission Disposal and the capability of Collision Avoidance Manoeuvre for active objects. Fragmentation events are modelled and propagated with the continuum approach implemented in the Starling suite. This tool has allowed extensive analyses in terms of the effects of the deployment of large constellations as well as different Post Mission Disposal strategies, as done by Muciaccia et al. in [50], identifying the most dangerous regions for operational spacecraft.

1.2. Aim of the thesis

As explained in this Chapter, the space debris environment and its evolution constitute a fundamental research topic for future access to space and for its sustainable use. It is of particular importance to be able to accurately model the distribution and propagation

of space debris in order to avoid catastrophic scenarios.
The aim of this thesis is the development of a continuum formulation to describe the evolution of the spatial density of debris clouds stemming from fragmentation events, based on the previous work of Letizia et al. [31]. Breakups are studied and modelled according to their nature (collisions or explosions). The focus of this study is the LEO region, hence the peculiarities of this orbital region are exploited in the modelling. To carry out this analysis, the idea of the probabilistic approach is followed, modelling debris clouds through the variation of their spatial density in time with the continuity equation. A study of the most accurate definition of the area-to-mass ratio bins in which the fragments are subdivided is conducted with the purpose of improving the accuracy of the model.
Then, a correct model of collision probability computation starting from the continuum formulation is developed, through an analogy with the kinetic theory of gases. Lastly, the effect of breakup events occurring at various altitudes and inclinations is studied according to a specific formulation of debris index. The resulting effect maps aim to analyse the effect of the addition of satellites in the already crowded LEO region and to identify the most dangerous orbital regions in LEO as well as the influence of constellations.
This thesis was part of the GREEN SPECIES project: "Robust control of the space debris population to define optimal policies and an economic revenue model for the sustainable development of space activities" (Grant agreement No. 101089265). This project is European Research Council (ERC) funded project under the European Europe research.

1.3. Contribution

The novel contributions of this thesis are listed here.

- The continuum formulation for the long-term propagation of debris clouds in LEO has been implemented using the model developed by Letizia as main reference [31]. In opposition to the reference model and to the extension of the method with the Starling suite [16], this work uses the formulation of the spatial density depending on the radial distance, extended to account for latitude. With this formulation, an analysis on the best definition and number of area-to-mass ratio bins is carried out, proposing a further definition with respect to the ones examined in the reference model. The fragmentation events are modelled with the NASA Standard Breakup Model [25].
- The collision probability computation has been implemented in analogy with gas kinetics following the approach of Letizia et al. [36]. However, in this work the

original model has been corrected in accordance with the work of Giudici et al. [18].

- One of the main purposes of this thesis is the application of the aforementioned models for the assessment of the severity of in-orbit breakups. This formulation is largely based on the works of Letizia et al. [38, 40, 41] and the THEMIS software [7]. Part of the index formulation used in these previous works has been applied to the formulation developed throughout this thesis and a novel approach to better characterise the severity of breakups at low altitudes is proposed.
- The maps generated with the method developed throughout this thesis are compared with the effect maps obtained with the CiELO method and with the THEMIS software. The purpose of the comparison is to assess whether this method allows to obtain comparable effect maps in a reduced computational time.

1.4. Structure of the thesis

After an overview of the problem, the work is organised as follows.
Chapter 2 is dedicated to the development of the continuum formulation for the long-term modelling of debris clouds in LEO. The application of the model to a reference breakup is also included in this Chapter. Chapter 3 introduces the model for the computation of collision probability, to assess the impact of a breakup on a given target spacecraft. Particular attention is given to the correction of the model with respect to previous versions. The results are presented to show how the characteristics of the target spacecraft affect the collision probability with a fragment cloud. Chapter 4 uses the model for the collision probability computation to generate maps assessing the severity of breakups occurring at various altitudes and inclinations. The results show the maps computed with two different methods. Lastly, Chapter 5 concludes the thesis with a summary of the work and the acknowledgment of the limits of the proposed formulations with the related future work to be conducted. Further details on the mathematical concepts used for the implementations can be found in Appendices A and B.

2 | Continuum formulation for a fragmentation event

In this Chapter, a continuum model is implemented using as reference the model developed in [34], in order to assess the time evolution of the debris cloud generated by either a collision or an explosion. The model has four main blocks (Figure 2.1):

- A breakup model, to characterise the fragments generated by the collision or the explosion, starting from the initial conditions of the event.
- Numerical propagation of the Keplerian elements of the fragments, until the continuum formulation proposed by McInnes [47] can be applied.
- Spatial density function, translating the orbital parameters of the fragments into a continuous function depending on altitude and latitude.
- Continuum propagation of the spatial density function, applying the analytic solution found in [34].

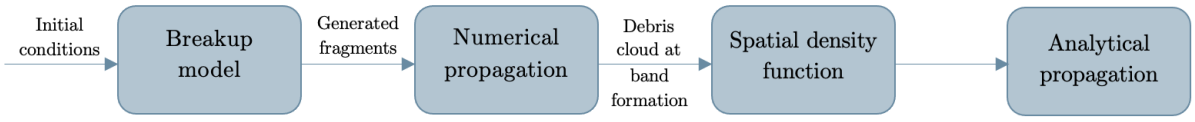

Figure 2.1: Block diagram of the continuum approach.

2.1. Breakup model

The first step of the method is the generation of a fragmentation event. The breakup model adopted for this purpose is the NASA Standard Breakup Model [25], which is a semi-empirical model capable of simulating the characteristics of the fragments generated after a collision or an explosion in space, given some initial conditions. The model defines the number, the size, the area-to-mass ratio (A/M) and the ejection velocity of all the

generated fragments [25], which are crucial elements for the continuum formulation. Since these parameters are not constant for all debris, they follow a distribution in characteristic length (L_c), which is taken as the independent variable to compute the characteristics for each fragment. Because of the use of distribution functions, different runs of the breakup model produce different debris clouds for the same initial conditions. The implementation of the breakup model used in this thesis can produce three kinds of fragmentation events: *catastrophic collisions*, *non-catastrophic collisions* and *explosions*. A collision is considered catastrophic when both the smaller and the larger objects are completely fragmented, that is when the impact energy per target mass exceeds 40 J/g [25].
According to the implementation of Johnson et al. [25], the number of fragments of size L_c or larger generated by an explosion can be computed as

$$N(L_c) = 6SL_c[\mathrm{m}]^{-1.6} \tag{2.1}$$

where S is a unitless scaling factor taking into account explosions from various explosive body types.
For both kinds of collisions instead, the number of fragments can be computed as

$$N(L_c) = 0.1M_e[\mathrm{kg}]^{0.75}L_c[\mathrm{m}]^{-1.71} \tag{2.2}$$

where M_e is the reference mass of the collision. Its definition is dependent on the type of collision:

$$\begin{aligned} \text{Catastrophic}: &\quad M_e[\mathrm{kg}] = M_t[\mathrm{kg}] + M_p[\mathrm{kg}] \\ \text{Non}-\text{catastrophic}: &\quad M_e[\mathrm{kg}] = M_p[\mathrm{kg}]v_c^2[\mathrm{km/s}] \end{aligned} \tag{2.3}$$

with M_t the target mass, M_p the projectile mass and v_c the relative impact velocity between the two. The expression for the reference mass in the non-catastrophic case has been corrected with respect to the one of Johnson et al. [25], following the approach adopted by Letizia [31].
The area-to-mass distributions of fragments follow lognormal distribution functions with mean value $\mu_{A/M}[\mathrm{m}^2/\mathrm{kg}]$ and standard deviation $\sigma_{A/M}[\mathrm{m}^2/\mathrm{kg}]$ according to the L_c value of each fragment. The model distinguishes between objects with L_c larger than 11 cm and smaller than 8 cm, while it employs a bridge function for objects in between. Moreover, the expressions for the parameters of the distribution differ for rocket bodies, spacecraft and small objects.
Likewise, the Δv distribution is modelled as a lognormal distribution depending on A/M,

with mean value $\mu_{\Delta v}[\mathrm{m}^2/\mathrm{kg}]$ and standard deviation $\sigma_{\Delta v}[\mathrm{m}^2/\mathrm{kg}]$. Different expressions are used for explosions and collisions. The distribution of the ejection velocity obtained with this model expresses the velocity magnitude [31], while the direction is considered to be isotropically distributed in direction similarly to Letizia et al. [34]. To guarantee the randomisation of the velocity vectors in space, the distribution of the impulse (Δv) must be multiplied by a directional distribution. This takes into account the fact that the longitude (λ) is uniformly distributed over $\lambda \in [0, 2\pi)$, while the latitude (β) has the following distribution [15]:

$$p_\beta = \frac{\cos\beta}{2}, \quad \beta \in \left[-\frac{\pi}{2}, \frac{\pi}{2}\right] \tag{2.4}$$

The ejection velocity vector can be written as a function of the two angles and of the magnitude Δv in the radial-transversal-out of plane (RSW) reference frame [15, 19]:

$$\boldsymbol{\Delta} v = \begin{Bmatrix} \Delta v \cos\beta \cos\lambda \\ \Delta v \cos\beta \sin\lambda \\ \Delta v \sin\beta \end{Bmatrix} \tag{2.5}$$

Note that the ejection velocity vector of some fragments deriving from a fragmentation event might be sufficient to inject them on a hyperbolic orbit with respect to the Earth [19]. However, these fragments are not of interest for the long-term assessment of the debris environment around the Earth, therefore they are not considered in the analysis. The details of the distributions used in the breakup model are reported in Appendix A.

2.2. Numerical propagation

This section concerns the phases of the evolution of the debris cloud immediately following the fragmentation event. In the initial phases, the continuum approach proposed by McInnes [46] cannot be applied because the effect of the Earth's oblateness is not accounted for, hence numerical propagation is required to follow the fragments [33]. The analytical formulation can be applied once the fragments have formed a band around the Earth, as explained in Section 2.2.2, allowing a more efficient computation.

2.2.1. Initial conditions

Once the fragments are generated, their orbital parameters can be retrieved from the NASA Standard Breakup Model. This provides the starting conditions for the numerical propagation carried out in the first phases of the cloud evolution using the Gauss' planetary equations, following the approach of Letizia et al. [33]. The Gauss' equations allow to propagate the trajectories of the fragments under the influence of atmospheric drag and the Earth's oblateness [69].
Given the parent orbit position and velocity vectors $\mathbf{r}_0$ and $\mathbf{v}_0$, the initial conditions of the generated fragments immediately after the breakup can be found considering that each fragment i is subject to an instantaneous velocity variation ($\boldsymbol{\Delta}v$) while sharing the same initial position as the parent orbit:

$$\mathbf{r}_i = \mathbf{r}_0, \quad \mathbf{v}_i = \mathbf{v}_0 + \boldsymbol{\Delta}v \tag{2.6}$$

Therefore, the fragments are ejected on their orbits according to the velocity variation [18]. Since the Gauss' equations are derived in terms of Keplerian elements $(a, e, i, \Omega, \omega, f)$, it is necessary to translate the information on the position and velocity of the fragments from Cartesian to Keplerian coordinates following the procedure in Curtis [8].

2.2.2. Cloud evolution and band formation

After the fragmentation, the evolution of the debris cloud in LEO is determined mainly by the perturbing forces of atmospheric drag and the Earth's oblateness, as the effects of SRP and third-body perturbation can be neglected. The evolution can be divided into three phases, as described by McKnight [48] and Jehn [22] (Figure 2.2). When a fragmentation occurs, debris are ejected in all directions. In the initial phase of the cloud evolution, the fragments remain close to each other forming an ellipsoidal cloud centred at the location of the parent satellite, as depicted in Figure 2.2a. At the moment of fragmentation, all fragments have the same position as the fragmentation location, yet their velocity - and therefore their energy - is different. For this reason, in the second phase of the evolution, the cloud is stretched along the orbit of the parent spacecraft forming torus around the Earth (Figure 2.2b). In this phase, the fragments are randomly distributed along the orbit, which means that the same density of fragments can be found for any mean anomaly $\overline{M}$ [14]. The notation $\overline{M}$ is introduced to avoid confusion with the mass M. The torus is then gradually dismantled in phase three, due to the different variations of right ascension of the ascending node (Ω) and argument of pericentre (ω) of each fragment caused by the Earth's oblateness. As a result, over the course of a few

years the debris cloud forms a band around the Earth (Figure 2.2c), whose latitude is limited by the maximum inclination of fragments (when the inclination is less than 90°). At this point in the evolution of the debris cloud, ω, Ω and the mean anomaly $\overline{M}$ are randomised and drag can be considered as the dominant perturbation in LEO [33].

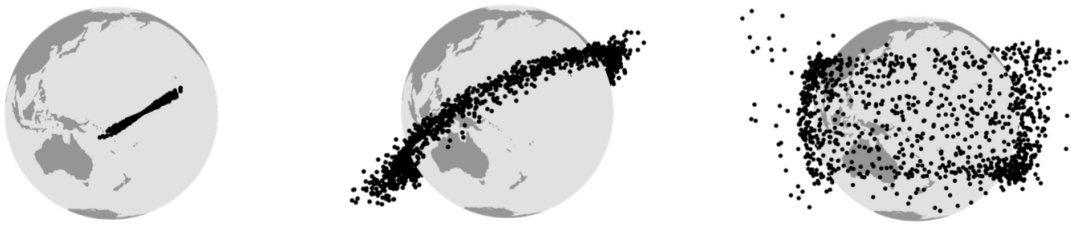

(a) Ellipsoid. (b) Toroid. (c) Band.

Figure 2.2: Phases of debris cloud evolution for a collision. Image from [31]

.

Until the time of *band formation*, the orbital parameters of the fragments are propagated with the Gauss' equations, with the formulation described in Section 2.2.3. The condition of band formation is reached when the angles $\overline{M}, \omega, \Omega$ have a uniform distribution between 0 and 2π [14].
The band formation time is estimated *a priori* based on the knowledge of the initial orbit, following the approach by Letizia et al. [33]. The time of band formation (T_b) is computed according to the analytical expression proposed by Ashenberg [2], by taking the maximum between the time of dispersion of the RAAN (T_Ω) and the one of the argument of pericentre (T_ω). However, since the analytical expression underestimates the real time required for band formation, the band formation time used in this work and in CiELO considers a safety factor with respect to the original formulation [33]. The final time is estimated as:

$$\begin{aligned} T_b &= 3\max(T_\Omega, T_\omega) \\ T_\Omega &= \frac{\pi}{3J_2\frac{R_E^2}{a^3}(7\cos i\cos\beta_\Omega + \sin i\cos u\sin\beta_\Omega)\Delta v} \\ T_\omega &= \frac{\pi}{3J_2\frac{R_E^2}{a^3}(7(2-\frac{5}{2}\sin i^2)\cos\beta_\omega + \frac{5}{2}\sin 2i\cos u\sin\beta_\omega)\Delta v} \end{aligned} \tag{2.7}$$

where $\mathrm{R_E}$ is the Earth's mean radius, i, a and u are respectively the inclination, the semi-major axis and the longitude of periapsis of the parent orbit and J_2 is the second zonal harmonic coefficient of the Earth's gravitational potential. Δv is the average velocity

variation caused by the breakup among all fragments [31], differently from Ashenberg [2] who assumed that the breakup could be modelled as an isotropic explosion, consequently causing all fragments to have the same Δv. β_Ω and β_ω are defined as

$$\begin{aligned} \tan\beta_\Omega &= \frac{1}{7}\tan i\cos u \\ \tan\beta_\omega &= \frac{5\sin 2i\cos u}{14(2-\frac{5}{2}\sin i^2)}. \end{aligned} \tag{2.8}$$

2.2.3. Numerical integration - King-Hele's formulation

The secular variation of the orbital elements of the fragments due to drag from the fragmentation event to the band formation is computed with the King-Hele's formulation [30]. The effect of aerodynamic drag is evaluated by using an exponential model for the density:

$$\rho = \rho_{ref}\exp\left(-\frac{h-h_{ref}}{H}\right) \tag{2.9}$$

where ρ is the density at altitude h, the reference value ρ_{ref} and the scale height H depend on the reference altitude h_{ref}, taken from Vallado [69]. h_{ref} is chosen as the closest tabulated value to the altitude of the breakup event, and it is kept constant during the propagation. Moreover, the effect of drag is considered up to 1000 km of altitude and a non-rotating atmosphere is assumed.
This implementation of the King-Hele's formulation follows the approach of Frey et al. [17], where adaptations were made to increase the accuracy of the model. Some parameters used in the formulation are introduced:

$$\begin{aligned} \delta &= c_d\frac{A}{M}, \quad z = \frac{ae}{H} \\ k_a &= \delta\sqrt{\mu_E a}\rho(h_p), \quad k_e = k_a/a \end{aligned} \tag{2.10}$$

where δ is the effective area-to-mass ratio, μ_E is the gravitational parameter, z is an auxiliary variable, c_d is the drag coefficient, which is assumed to be constant and equal to 2.2 for all fragments [69], and $\rho(h_p)$ is the density evaluated at perigee altitude:

$$\rho = \rho_{ref}\exp\left(-\frac{h_p-h_{ref}}{H}\right) = \rho_{ref}\exp\left(-\frac{a-R_h}{H}\right)\exp(z) \tag{2.11}$$

with $R_h = R_E + h_{ref}$. The variation of semi-major axis a and eccentricity e is defined

according to the eccentricity value of each fragment, considering four ranges:

- $e < 0.001$

$$\begin{aligned} \frac{da}{dt} &= -k_a \\ \frac{de}{dt} &= 0 \end{aligned} \tag{2.12}$$

- $0.001 \leq e < 0.01$

$$\begin{aligned} \frac{da}{dt} &= -k_a \exp(-z)[I_0 + 2eI_1] \\ \frac{de}{dt} &= -k_e \exp(-z) \left[I_1 + \frac{e}{2}(I_0 + I_2)\right] \end{aligned} \tag{2.13}$$

- $0.01 \leq e < 0.2$

$$\begin{aligned} \frac{da}{dt} &= -k_a \exp(-z) \left[I_0 + 2eI_1 + \frac{3}{4}e^2(I_0 + I_2) + \frac{e^3}{4}(3I_1 + I_3)\right] \\ \frac{de}{dt} &= -k_e \exp(-z) \left[I_1 + \frac{e}{2}(I_0 + I_2) + \frac{e^2}{8}(-5I_1 + I_3) + \frac{e^3}{16}(-5I_0 - 4I_2 + I_4)\right] \end{aligned} \tag{2.14}$$

- $0.2 \leq e < 1$

$$\begin{aligned} \frac{da}{dt} &= -k_a c_a [\mathbf{r}^T \mathbf{K}_a \mathbf{e}] \\ \frac{de}{dt} &= -k_e c_e [\mathbf{r}^T \mathbf{K}_e \mathbf{e}] \end{aligned} \tag{2.15}$$

with

$$c_a = \sqrt{\frac{2}{\pi z}} \frac{(1+e)^{3/2}}{(1-e)^{1/2}}, \quad c_e = \sqrt{\frac{2}{\pi z}} \left(\frac{1+e}{1-e}\right)^{1/2} (1-e^2) \tag{2.16}$$

and

$$\begin{aligned} \mathbf{e}^T &= (1 \quad e \quad e^2 \quad e^3 \quad e^4), \\ \mathbf{r}^T &= \left(1 \quad \frac{1}{(z(1-e^2)} \quad \frac{1}{z^2(1-e^2)}\right), \end{aligned} \tag{2.17}$$

and

$$\mathbf{K}_a = \begin{bmatrix} 1/2 & 1/16 & 9/256 \\ 0 & -1/2 & -3/16 \\ 0 & 3/16 & 75/128 \\ 0 & 0 & 3/16 \\ 0 & 0 & -15/256 \end{bmatrix}, \quad \mathbf{K}_e = \begin{bmatrix} 1/2 & -3/16 & -15/256 \\ 0 & -1/4 & 9/32 \\ 0 & 3/16 & 39/128 \\ 0 & 0 & 3/32 \\ 0 & 0 & -15/256 \end{bmatrix}. \tag{2.18}$$

I_k is the modified Bessel function of the first kind, order k and argument z:

$$I_k(z) = \frac{1}{\pi} \int_0^{\pi} e^{z \cos\theta} \cos(k\theta)\, d\theta \quad k \in \mathbb{Z} \tag{2.19}$$

As for the Earth's oblateness, its secular effect is included in the Gauss' planetary equations in terms of the zonal harmonic J_2. This is due to two reasons, as originally explained by Letizia et al. [31]: firstly, the Earth's oblateness affects only ω and Ω over the long-term, hence a highly precise description is not necessary. Secondly, the transition of the debris cloud from a ring to a torus around the Earth is described by Ashenberg [2] considering only the effect of J_2 in order to estimate the duration of the process. Therefore, the variation of orbital parameters caused by J_2 is evaluated with the following equations:

$$\begin{aligned} \frac{d\omega}{dt} &= \frac{3}{2} J_2 \frac{R_E^2}{p^2} \overline{n} \left(2 - \frac{5}{2} \sin i^2 \right) \\ \frac{d\Omega}{dt} &= -\frac{3}{2} J_2 \frac{R_E^2}{p^2} \overline{n} \cos i \end{aligned} \tag{2.20}$$

where $p = a(1 - e^2)$ is the semi-latus rectum of the orbit and $\overline{n} = \sqrt{\mu_E / a^3}$ is the mean motion.

The orbital parameters of the fragments are numerically integrated with the set of equations given by Eqs. 2.12-2.20 from the fragmentation to the time of band formation T_b. The propagation is stopped with an event function when the perigee altitude h_p falls below 50 km, since in this case the fragment is considered to be re-entering through the atmosphere [31, 34]. As for the inclination, it remains constant for each fragment throughout the simulation. The considered perturbations do not affect it due to the assumption of non-rotating atmosphere.

The values of the true anomaly f of the fragments at the end of the propagation can be retrieved from $\overline{M}$. Particularly, the model computes random values of $\overline{M}$ between 0 and 2π for each fragment, then these values are transformed into the corresponding values of

f according to the range of eccentricity to which each fragment belongs [69]:

- $e < 0.2$:

$$f = \overline{M} + \left(2e - \frac{1}{4}e^3\right)\sin\left(\overline{M}\right) + \frac{5}{4}e^2\sin\left(2\overline{M}\right) + \frac{13}{12}e^3\sin\left(3\overline{M}\right) + O(e^4) \tag{2.21}$$

- $e \geq 0.2$

$$\begin{cases} \overline{M} = E - e\sin E \\ \tan\frac{f}{2} = \sqrt{\frac{1+e}{1-e}}\tan\frac{E}{2} \end{cases} \tag{2.22}$$

For high eccentricities the computational effort required to solve the system of equations for each fragment is higher than for lower eccentricities, where a series expansion allows to accelerate the computational procedure.

2.3. Spatial Density Function

Once the band formation has occurred, the information on the single fragments can be translated into a continuous density function, which depends only on the Keplerian elements of the fragments. The spatial density retrieved through this approach will serve as the initial condition for the analytical propagation. The expression used for the spatial density function derives from Kessler's work [27]:

$$N(r, \beta) = n(r)f(\beta) \tag{2.23}$$

where $n(r)$ and $f(\beta)$ are the components of the spatial density accounting for, respectively, the dependence on the radial distance r and on latitude β, defined as:

$$n(r) = \frac{1}{4\pi^2 r a^2}\frac{1}{\sqrt{e^2 - (\frac{r}{a} - 1)^2)}} \tag{2.24}$$

$$f(\beta) = \frac{2}{\pi}\frac{1}{\sqrt{\cos^2\beta - \cos^2 i}} \tag{2.25}$$

provided that

$$\begin{aligned} &r_p < r < r_a \\ &0 < \beta < i \end{aligned} \tag{2.26}$$

With r_p pericentre, r_a apocentre and i inclination of the fragment orbit. When $r < r_p, \quad r > r_a$, or $\beta > i$, $N(r, \beta) = 0$. Note that the latitude β is linked to the inclination i by spherical geometry, particularly by the sine rule:

$$\sin \beta = \sin u \sin i \tag{2.27}$$

with $u = \omega + f$ argument of latitude of the fragment.
The resulting expression of the spatial density function represents the probability of finding a particle, at a certain distance from the central body r and at a certain latitude β knowing the semi-major axis a, the eccentricity e and the inclination i, assuming the other parameters are randomly distributed [33]. However, Eq. 2.23 cannot be applied directly to the cloud, using the initial values of a, e and i of the orbit where the fragmentation has taken place, as the energy distribution among fragments after the breakup has to be accounted for. To do this, the spatial density function has to be applied to each fragment in the fragmentation cloud, then the total density function is found by considering the contribution of each fragment:

$$N(r, \beta) = \sum_{i=1}^{N_b} N_i(r, \beta) \tag{2.28}$$

where N_b is the number of fragments in the fragment cloud at the time of band formation.

2.4. Continuum formulation

Once the initial spatial density function is known at the band formation, the continuity equation is used to derive the evolution of the fragment spatial density in time, under the effect of atmospheric drag. The continuity equation can be written as:

$$\frac{\partial n}{\partial t} + \nabla \cdot (n\mathbf{f}) = \dot{n}^+ - \dot{n}^-, \tag{2.29}$$

where n is a generic density function, while $\nabla \cdot (n\mathbf{f})$ models atmospheric drag [47]. Here, no discontinuous events are considered, hence $\dot{n}^+ - \dot{n}^- = 0$, as in [31]. The following derivation of the analytical solution to the continuity equation takes into account only the expression of the spatial density function depending on the radial distance ($n(r)$). However, the non-linear dependency of the spatial density function on latitude does not modify the solution as it is only a multiplicative factor, hence the analytical solution holds also for the expression of the spatial density function acounting for latitude ($N(r, \beta)$ as

in Eq. 2.23) which will be used throughout this thesis.
Since the spatial density depends on the radial coordinate r, a spherical symmetry is assumed. The propagation with the analytical solution to the continuity equation is applicable only after the moment of band formation due to this assumption and to the fact that atmospheric drag is the only considered perturbation. With a spherical symmetry, the vector field has only one component:

$$f_r = v_r \tag{2.30}$$

where v_r is the drift velocity in the radial direction, obtained from the drag acceleration

$$a_d = \frac{1}{2}\frac{c_d A}{M}\rho(r)v^2 \tag{2.31}$$

with c_d the drag coefficient. A is the fragment cross-sectional area, M is the fragment mass, v is the fragment velocity and $\rho(r)$ is the atmospheric density computed with Eq. 2.9. The variation of orbital energy ξ caused by drag is

$$\frac{d\xi}{dt} = \frac{\mu_E}{2r^2}v_r \tag{2.32}$$

or, alternatively

$$\frac{d\xi}{dt} = -v_\theta a_d \tag{2.33}$$

where v_θ is the transversal velocity. At this point, an assumption regarding the geometry of the problem has to be made in order to retrieve an analytical solution to the continuity equation. This is the hypothesis of quasi-circular orbits for the fragments in the band. Although this assumption limits the applicability of the method, it does not imply a significant loss of accuracy in LEO. Under this hypothesis, v_θ can be computed as

$$v_\theta \approx \sqrt{\frac{\mu_E}{r}}. \tag{2.34}$$

Combining Eqs. 2.32 and 2.33, the radial velocity can be written as

$$v_r = -2r^2\frac{v_\theta a_d}{\mu_E}. \tag{2.35}$$

Substituting a_d and v_θ with their expressions in Eqs. 2.31 and 2.34 and considering $v^2 =$

$v_\theta^2 + v_r^2 \approx v_\theta^2$, the radial velocity can be expressed as

$$v_r = -\sqrt{\mu_E r} c_d \frac{A}{M} \rho(r). \tag{2.36}$$

Following the approach of Letizia [31], the parameter ϵ is introduced

$$\epsilon = \sqrt{\mu_E} \frac{c_d A}{M} \rho_{ref}. \tag{2.37}$$

ϵ collects all the terms not depending on r. The expression has been slightly modified with respect to the original one by McInnes [47] to improve numerical accuracy. The final expression for v_r can be obtained, putting $R_h = R_E + h_{ref}$

$$v_r = -\epsilon \sqrt{r} \exp(-\frac{r - Rh}{H}). \tag{2.38}$$

Eq. 2.38 allows to develop the term $\nabla \cdot (n\mathbf{f})$ in the continuity equation, which can be rewritten as

$$\frac{\partial n(r,t)}{\partial t} + \frac{1}{r^2} \frac{\partial}{\partial r} [r^2 v_r n(r,t)] = 0. \tag{2.39}$$

Lastly, by differentiating and collecting terms, Eq. 2.39 becomes

$$\frac{\partial n(r,t)}{\partial t} + v_r \frac{\partial n(r,t)}{\partial r} + (\frac{2}{r} v_r + v_r') n(r,t) = 0 \tag{2.40}$$

where $(\cdot)'$ stands for the derivative with respect to r.
As explained in Section 1.1.1, this first order PDE can be solved with the method of characteristics[1]. The solution, obtained with the approximation $\sqrt{r} \approx \sqrt{R_h}$, is given by

$$G(r,t) = \exp\left(\frac{r - R_h}{H}\right) + \epsilon \frac{\sqrt{R_h}}{H} t. \tag{2.41}$$

The final explicit expression for the density evolution, found in [47], can then be obtained

$$n(r,t) = \frac{\Psi[(G(r,t)]}{r^2 v_r} = \frac{\Psi\left\{\exp[\frac{r-R_h}{H}] + (\epsilon\sqrt{R_h}/H)t\right\}}{-\epsilon r^{5/2} \exp[-\frac{r-R_h}{H}]}. \tag{2.42}$$

The function Ψ is derived from the initial condition $n(r, t = 0)$ and from the characteristics at $t = 0$, defining the independent variable z

[1]The full application of the method of characteristics to the continuity equation is detailed in Appendix B.

$$z = G(r,0) = \exp\left(\frac{r - R_h}{H}\right) \tag{2.43}$$

Leading to

$$\Psi(z) = n(r,0)[r^2 v_r(r)] = n(H\log z + R_h, 0)[-\epsilon z^{-1}(H\log z + R_h)^{5/2}] \tag{2.44}$$

Eq. 2.42 provides a fully analytical solution to the continuity equation, able to determine the effect of drag on the global debris cloud. However, the distribution in area-to-mass ratio (A/M) of the fragments generates significantly different values of the parameter ϵ as defined in Eq. 2.37. Therefore, to improve the accuracy of the method, the fragments are divided into an appropriate number of A/M bins [31], as explained in Section 2.5. Then, the analytical solution is applied to each A/M bin separately, using an average value ϵ_i. The corresponding partial densities n_i are summed to obtain the global cloud density

$$n(r,t) = \sum_i n_i = \sum_i \frac{\Psi[(G(r,t)]}{r^2 v_r} = \frac{\Psi\left\{\exp[\frac{r-R_h}{H}] + (\epsilon_i\sqrt{R_h}/H)t\right\}}{-\epsilon_i r^{5/2}\exp[-\frac{r-R_h}{H}]}. \tag{2.45}$$

As previously mentioned, the solution in Eq. 2.45 is valid also for the evolution of the spatial density depending on the radial distance r and on latitude β, provided that Ψ is obtained with the expression of $N(r,\beta,t)$.

2.5. A/M bins definition

To improve the accuracy of the analytical propagation, it is necessary to subdivide the fragments in A/M bins, which should guarantee an accurate representation of the distribution of the fragments. Three possible definitions for A/M bins have been taken into consideration and have been tested:

- *same fragment number*: each bin contains the same number of fragments at the band formation,
- *logarithmically spaced*: the bins have logarithmically spaced edges, whose bounds are the maximum/minimum A/M of the fragment population at band formation,
- *constant* $\Delta A/M$: the bins are spaced with a constant $\Delta A/M$, where the bounds are the maximum/minimum A/M of the fragment population at band formation.

The first two definitions were previously tested also by Letizia et al. in [34]. To evaluate the most accurate definition, two indicators have been considered to compare the results of

the analytical method (n_A) and of the numerical method (n_N) (which is implemented with the numerical propagation for each fragment according to the King-Hele's formulation as in Section 2.2.3):

- err_{frag}, which is the relative error of the total number of fragments

$$err_{frag} = \frac{|\int n_A dh - \int n_N dh|}{\int n_N dh}, \tag{2.46}$$

- err_{prof}, which is the absolute error between the two density profiles

$$err_{prof} = \frac{\int |n_A - n_N| dh}{\int n_N dh}. \tag{2.47}$$

The two errors have been selected in order to have a relative metric, err_{frag}, which has a precise physical meaning, and an absolute metric, err_{prof}, which is similar to a mean squared error. The analytical method is considered acceptable when err_{prof} and err_{frag} are, respectively, below 0.2 and 0.1 [31]. First, the debris cloud is propagated both with the analytical method using 10 A/M bins and with the numerical one, then the two errors are computed at the end of the propagation to determine the best A/M bins definition and for the best definition the optimal number of A/M bins to use is retrieved.

2.5.1. Optimal bin definition

To test the optimal bin definition and the optimal number of A/M bins, a reference case has been used. It is the small breakup of Cosmos 1867, whose characteristics have been retrieved from [31] and can be found in Table 2.1.

Table 2.1: Cosmos 1867 breakup characteristics.

h_p [km]	h_a [km]	i_0 [deg]	M_e [kg]	N_F [-]
775	800	65	2.665	28136

M_e is the reference mass for a non-catastrophic collision (see Section 2.1) and N_F is the number of generated fragments. Fragments with a lower size limit of 1 mm have been considered and a relative impact velocity of 1 km/s has been used.
As explained in Section 2.5, the first step in determining the best definition of A/M bins is considering 10 bins for all the three cases. Consequently, the errors according to the two metrics in Section 2.5 are computed to identify the optimal definition for the bins. Since

the NASA Standard Breakup Model provides different characteristics of the breakup at each run, more reliable results can be obtained by using multiple runs of the model and averaging the outcome. For this reason, for all three definitions of A/M bins with 10 bins, 10 runs of the breakup model are used. For each run, the spatial density of the generated debris cloud is propagated for 1000 days (from the time of band formation), then the profile error and the fragment number error between the analytical model and the numerical one obtained with the King-Hele's formulation are computed. Lastly, the mean errors are calculated. The results can be seen in Figure 2.3 and Figure 2.4.

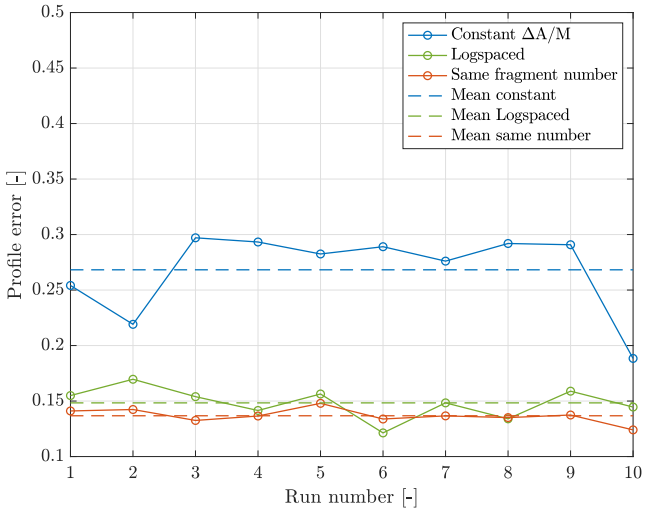

Figure 2.3: Error on the density profile for ten runs of the NASA Standard Breakup Model after 1000 days of propagation.

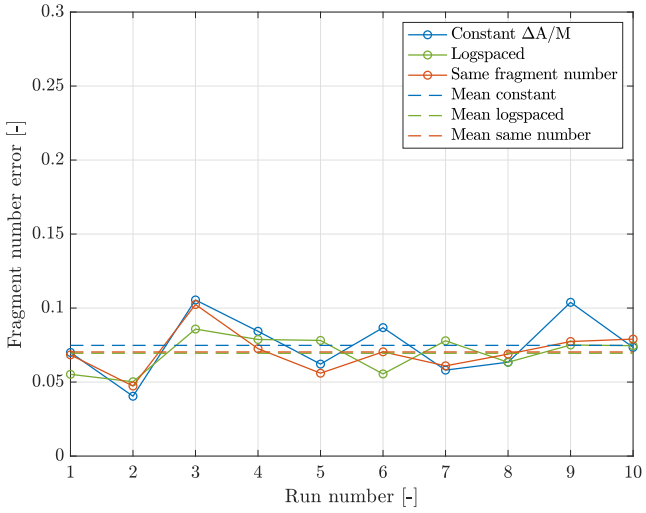

Figure 2.4: Error on the fragment number for ten runs of the NASA Standard Breakup Model after 1000 days of propagation.

The average profile and fragment number errors for the three cases are listed in Table 2.2.

Table 2.2: Average errors for the three bin definitions

	Constant $\Delta A/M$	Logspaced	Same fragment n°
$\overline{err}_{prof}$	26.8%	14.8%	13.7%
$\overline{err}_{frag}$	7.5%	6.95%	7.03%

From the average profile error, one can notice that using bins with the same number of objects gives the most accurate results, although using logspaced bins provides similar results. The average fragment number error instead shows that logspaced bins are more suited for an accurate representation, however bins with the same number of objects present only a slightly higher error. Therefore, the two metrics used for the evaluation of the best definition of A/M bins essentially indicate an equivalence between logspaced bins and bins with the same number of fragments. As for bins with a constant $\Delta A/M$, the two errors show that they lead to higher inaccuracies and non acceptable results. To reach the same level of accuracy of the other two definitions, many more A/M bins are required, which means a higher computational cost and a smaller A/M step. This is particularly interesting because from a theoretical standpoint, using bins with a constant $\Delta A/M$ should be the preferred definition as it guarantees the same accuracy for the description of the dynamics of each fragment, both with large and small A/M. The other two definitions instead follow the distribution of the fragments rather than their dynamics, hence they are able to capture the lognormal A/M distribution of the fragments. Therefore, these two definitions provide higher accuracy for fragments with smaller A/M ratios, which are the majority of the fragments generated by the breakup, ultimately leading to a smaller overall error, well within the thresholds for the analytical method to be acceptable.

2.5.2. Optimal bin number

Once the best definitions for A/M bins have been selected, an analysis on the optimal number of bins to use is carried out. The optimal bin number is a trade-off between accuracy and computational cost. For bins with the same number of objects and logspaced bins, the two errors (err_{prof} and err_{frag}) are computed by considering a number of bins ranging from 1 to 15. 15 bins have been set as the limit to avoid increasing the computational effort unnecessarily. Also in this analysis, 10 runs of the NASA Standard Breakup Model have been used to have more general results, therefore the errors with 1 to 15 A/M bins have been computed as the average errors obtained in 10 runs.

The results for logspaced bins can be found in Figure 2.5.

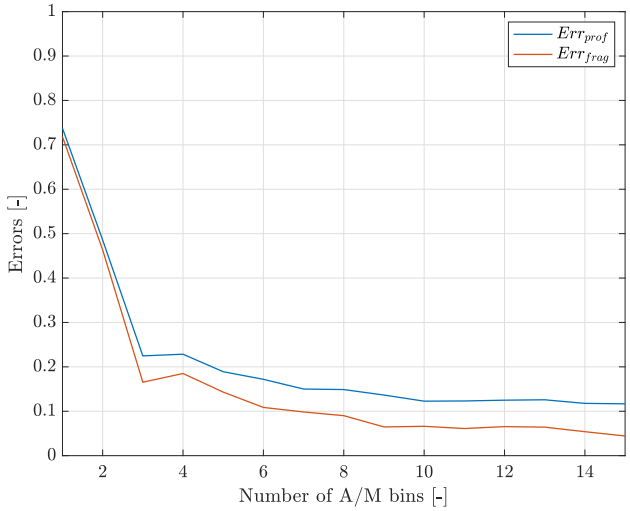

Figure 2.5: Profile error and fragment number error for logspaced bins from 1 to 15 bins.

The plot shows that for both metrics, the error is very high when using a small number of bins, then it decreases and it reaches a plateau around 10 bins. This means that using 10 bins is sufficient to guarantee an accurate representation while maintaining a small error. For bins with the same number of objects instead, the results (obtained with 10 different runs of the breakup model) are depicted in Figure 2.6.

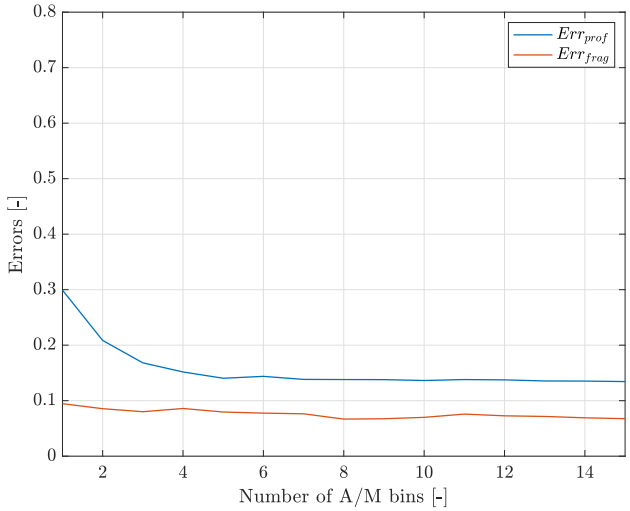

Figure 2.6: Profile error and fragment number error for bins with the same number of fragments, from 1 to 15 bins.

The profile error shows the same behaviour observed with the logspaced bins, i.e. it is

high with a low number of bins, then it decreases until it reaches a plateau at around 10 bins. The fragment number error curve instead does not exhibit such a well defined behaviour. Although the error tends to decrease with a growing number of bins, it is low even with only one A/M bin, at around 0.1. For this reason, it is worth studying how the error on the number of fragments is affected by the altitude of the breakup. To this aim, the fragment number error with respect to the number of bins has been computed by considering different altitudes for the perigee of the parent orbit, while the eccentricity and inclination are the same as Cosmos 1867. The results can be seen in Figure 2.7.

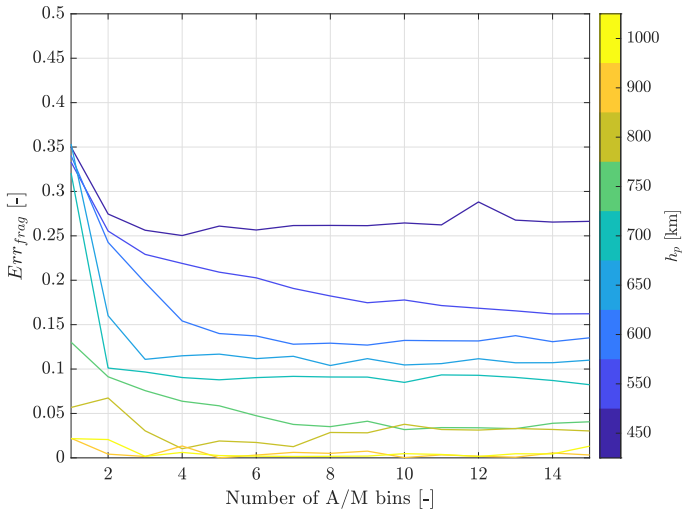

Figure 2.7: Fragment number error for bins with the same number of fragments, from 1 to 15 with respect to the altitude of fragmentation.

The plot shows a clear correlation between the error and the altitude at which the breakup occurs. Specifically, the higher the altitude of the breakup, the lower the error. With this in mind, it is safe to assume that also for the bins with the same number of objects 10 bins should be enough to have an accurate description. In fact, also for the worst case scenario (i.e. the lowest altitude), at 10 bins the error reaches a plateau. It is important to mention that the continuum approach has been validated for altitudes between 700 km and 1000 km, while these results have been obtained by extending the analytical model below 700 km. As shown by Letizia [32], the analytical approach does not provide accurate results below 700 km, and its extension must be carried out with the use of the finite difference scheme. This is the reason for the high value of the error at low altitudes. However, the aim of the plot in Figure 2.7 is to show the trend of the error on the number of fragments. Moreover, the behaviour of the curves does not appear smooth as a result of the averaging over 5 runs of the breakup model.

Although the previous results have demonstrated an equivalence in accuracy between bins with the same fragment number and logspaced bins, all the results presented in this thesis will refer to bins with the same number of fragments.

2.6. Results

This section presents the results obtained with the application of the continuum approach. The same Cosmos 1867 breakup studied for the analysis of the A/M bins is exploited, in order to follow the evolution of its debris cloud in time.

The considered scenario involves the non-catastrophic collision between a 1500 kg spacecraft and a 2.665 kg projectile mass, with a relative velocity of 1 km/s. The fragmentation modelled with NASA Standard Breakup Model considers fragment sizes ranging from 1 mm to 10 cm and a maximum velocity variation of 10 km/s. The characteristics of the breakup are summarised in Table 2.3.

Table 2.3: Breakup characteristics

h_p [km]	h_a [km]	i_0 [deg]	e [-]	N_F [-]	T_B [days]
775	800	65	0.0017	28136	483

By computing the impact energy per target mass [25]:

$$\tilde{E}_p = \frac{m_p v_{rel}^2}{2m_t} \tag{2.48}$$

one obtains $\tilde{E}_p$=0.88 J/g. Recalling from Section 2.1 that a collision is considered catastrophic when the specific impact energy is above 40 J/g, it is clear that this scenario represents indeed a non-catastrophic collision.
Figure 2.8 shows the distribution of the fragments right after the fragmentation in terms of A/M and velocity variation, from the NASA Breakup model.

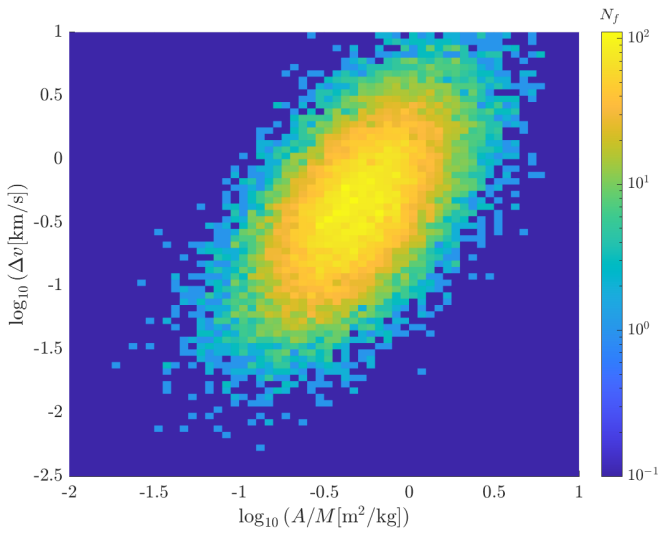

Figure 2.8: Distribution of area-to-mass ratio and velocity variation of the fragments generated in the Cosmos 1867 breakup.

A typical diagram employed to represent the distribution of the fragments generated in a breakup is the Gabbard diagram [57]. The classical representation of the diagram plots the apocentre and pericentre altitudes of the generated fragments as a function of the orbital period, producing a typical X shape centred at the breakup location, as shown in Figure 2.9.

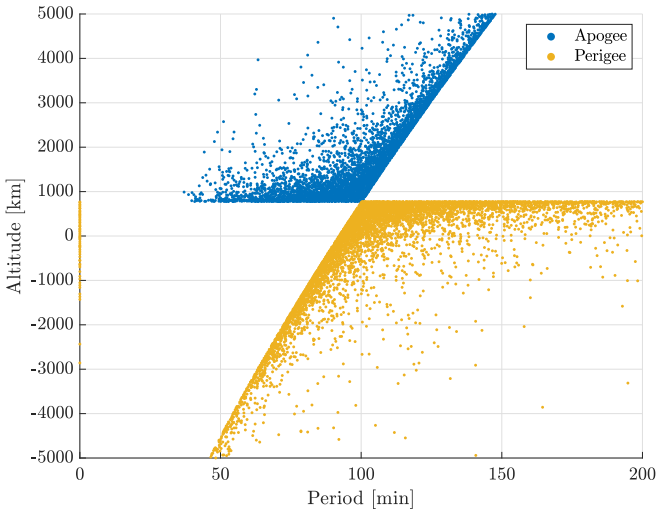

Figure 2.9: Gabbard diagram right after the fragmentation: apocentre and pericentre distribution as a function of the orbital period.

One can notice that some fragments exhibit a negative altitude of pericentre, hence these

fragments are bound to re-enter in the atmosphere. An alternative representation of the Gabbard diagram is also presented, both right after the fragmentation (Figure 2.10a) and at the band formation (Figure 2.10b), indicating the number of fragments in each bin of the semi-major axis and eccentricity grid on a logarithmic scale.

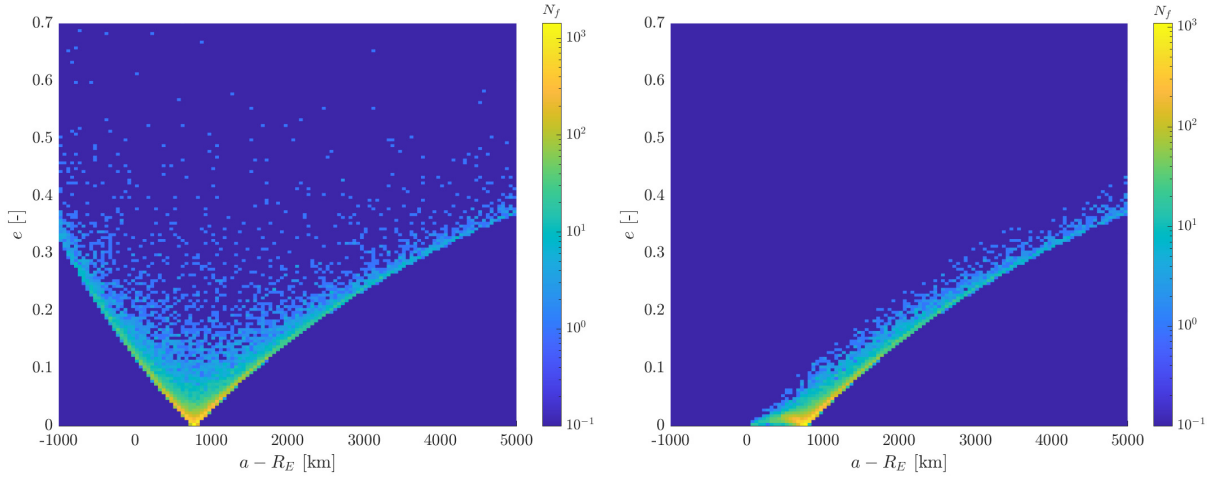

(a) Alternative Gabbard diagram at fragmentation. (b) Alternative Gabbard diagram at band formation.

Figure 2.10: Alternative representation of the Gabbard diagram right after the fragmentation (a) and at the moment of band formation (b).

Figure 2.10a shows a typical V-shaped distribution centred at the altitude and eccentricity of the breakup. The left leg of the plot represents the fragments whose semi-major axis decreases and whose apogee remains at the breakup location, while the right leg of the plot accounts for the fragments whose perigee is at the breakup location and whose semi-major axis increases. The effect of atmospheric drag can be seen in the reduction in apogee over time, leading to the distribution at the band formation (Figure 2.10b). This result is particularly pronounced for fragments with semi-major axis values below 1000 km, resulting in a circularisation of their orbits. At band formation, the left leg of the Gabbard diagram disappears because of fragments re-entering the atmosphere due to drag. This is to be expected as the fragments on the left leg have perigees located at lower altitudes, hence they are more affected by drag, eventually falling and re-entering in the atmosphere.

After band formation, the continuum approach has been used. The spatial density function of the debris cloud has been computed at the moment of band formation, subdividing the fragments into 10 A/M bins, whose mean values are reported together with the initial spatial density of the cloud in Figure 2.11. The radial distance has been discretised into bins of 50 km width.

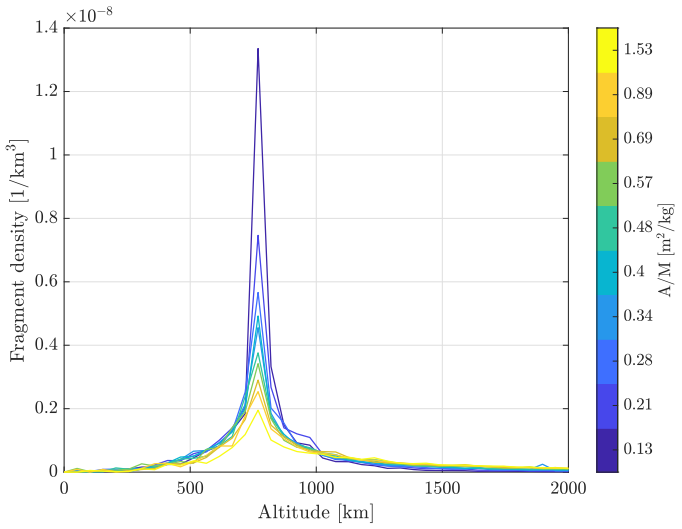

Figure 2.11: Spatial density function of the debris cloud at band formation.

The evolution in time of the spatial density of the debris cloud has been evaluated with the analytical solution for a timespan of 1000 days after the band formation. The result is shown in Figure 2.12.

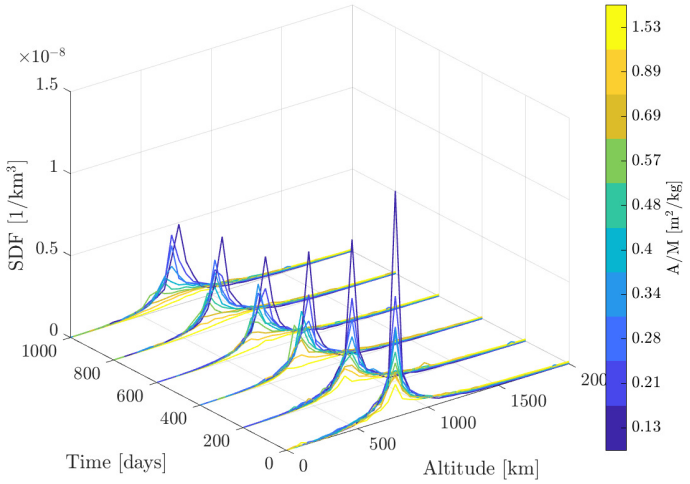

Figure 2.12: Evolution of the spatial density of the debris cloud in time starting from the band formation.

Moreover, an analysis on the position of the altitude of the peak for each A/M bin is carried out and shown in Figure 2.13.

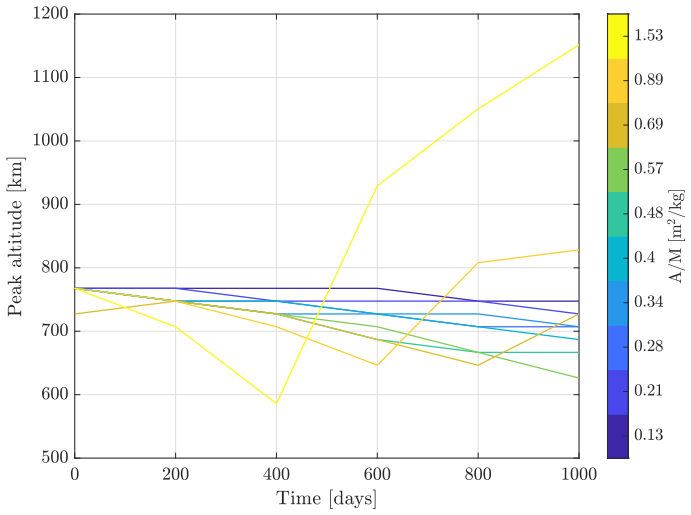

Figure 2.13: Evolution of the peak altitude for each area-to-mass ratio bin.

Figure 2.13 shows that the location of the peak undergoes some fluctuations for fragments with high A/M as the curves become flatter. This is due to the effect of drag, which is more pronounced at lower altitudes, where the density experiences a more significant reduction. The peak initially shifts towards low altitudes, where the density is reduced to the point of becoming smaller than the density at higher altitudes, which explains the new peaks moving to higher altitudes.

Lastly, the evolution of the overall density is depicted in Figure 2.14. It is important to stress that, even though for some A/M bins there is no definite decrease in the peak of spatial density, when looking at the total density there is a distinct decrease of the peak in time. The overall behaviour of the density is shown as it is crucial for the collision probability computation, as will be explained in Chapter 3.

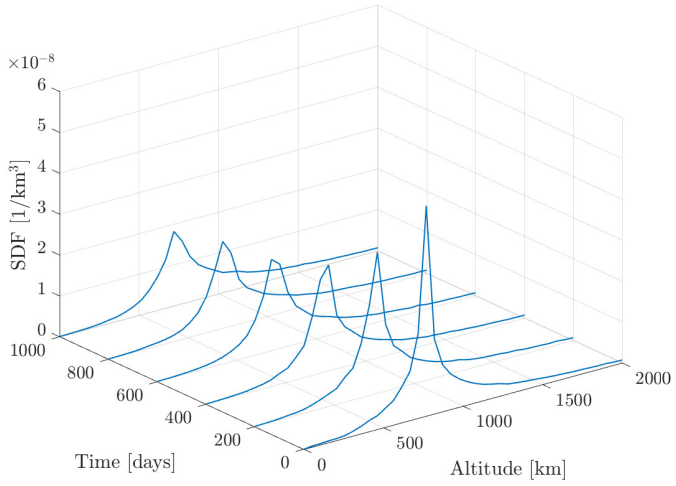

Figure 2.14: Spatial density function of the debris cloud at band formation.

2.6.1. Computational comparison

An additional analysis in terms of computational time has been carried out for the analytical method. The breakup of Cosmos 1867 is propagated from the moment of fragmentation to 1000 days after the band formation, both with the analytical and numerical methods, with a time step of 1.5 days. The numerical approach propagates the trajectory of each single fragment with the same propagator described in Section 2.2.3, i.e. with the King-Hele's formulation. The results for the computational times of the MATLAB codes implemented without parallelisation, averaged over 5 runs, for a PC with an Intel Core i7 at 2.3 GHz, can be found in Table 2.4.

Table 2.4: Average computational times for the analytic and numerical methods.

	NASA breakup	Band formation	Propagation
Analytic	39.0 s	60.4 s	4.45 s
Numerical	39.0 s	60.4 s	99.8 s

For both methods, the time required for the generation of the cloud and for the propagation until band formation is the same. However, the propagation until band formation is the most demanding contribution for the analytic approach, whereas for the numerical method the full propagation is computationally heavier since it depends on the number of fragments in the cloud. The results of the comparison clearly highlight the advantage of

the analytical approach with respect to the numerical one, due to the significant reduction in the computational time needed for a full propagation.

3 | Collision Probability

In this Chapter, the consequences of fragmentation events are studied by evaluating the collision probability for spacecraft crossing the debris clouds. The collision probability can be related to the spatial density of the cloud using a simplified model. This allows to add a further block to the continuum propagation block diagram (Figure 3.1).

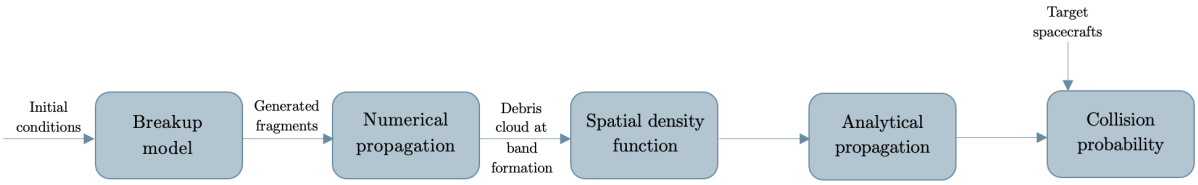

Figure 3.1: Building blocks of the continuum approach with the collision probability computation.

3.1. Analogy with gas kinetics

The collision probability can be computed in analogy with the kinetic theory of gases [48, 66]. The cumulative collision probability with a target is computed according to a Poisson distribution associated with gas kinetics [23], assuming that collisions between a target and the background debris population can be modelled as collisions among the molecules of an inert gas. As explained by Letizia [31], rare events can be modelled as a Poisson process provided that certain hypotheses are respected. Specifically, given N_E events occurring in the time interval $\Delta t = [0, t]$ (with subintervals Δt_H), the hypotheses are the following:

- $N_E(0) = 0$,
- the events happening in a time interval are probabilistically independent from the ones occurring in other intervals,
- the probability of collision in a time interval is proportional to the duration of the interval,

- the probability of exactly one event happening in a time interval Δt_H is equal to the product of the interval length and the rate of the Poisson process plus a small quantity with respect to Δt_H,
- the probability of multiple events happening in a time interval is small.

As pointed out by Jenkin [23], the second condition is satisfied by the random motion of the molecules due to repeated collisions. In the same way, there is little correlation between the motion of the satellite and that of the background population, hence the analogy with gas molecules is permitted. However, in the first phases of the evolution of the debris cloud, the motion of the fragments cannot be assimilated to the one of molecules as the fragments move in a highly correlated manner. For this reason, the analogy is applied only to the last phases of the cloud evolution, once the fragments have formed a band around the Earth and their motion can be considered random. The third hypothesis is related to the availability of a large number of fragments [31]. Moreover, this method assumes no interaction among the fragments in the debris cloud [31].
With these ideas in mind, the cumulative collision probability with the target can be computed as:

$$p_c(t) = 1 - \exp\left(-N_c(\Delta t)\right) \tag{3.1}$$

where N_c is the cumulative number of collisions in the time interval Δt. N_c can be estimated from the integral mean of the impact rate ($\overline{\dot{\eta}}$) between the debris cloud and the target satellite, whose computation is detailed in Section 3.2. Therefore, the cumulative number of collisions in the time interval Δt, considering the average impact rate over an orbit, can be found as:

$$N_c(t) = \overline{\dot{\eta}} \Delta t. \tag{3.2}$$

3.2. Impact rate and collision velocity estimation

The impact rate is the main quantity needed for the estimation of collision probability. The average impact rate over a target orbit can be computed as [36]:

$$\overline{\dot{\eta}} = \sigma_c N(r, \beta, t) \overline{v}_{rel} \tag{3.3}$$

where $N(r, \beta, t)$ is the spatial density of the debris cloud, taking into account the expression as a function of the radial distance and latitude for increased accuracy in the estimation of the impact rate, $\overline{v}_{rel}$ is the average impact velocity, σ_c is the collisional cross-sectional area. Following the approach of Letizia et al. [36], σ_c is defined as the

target spacecraft area A_T since the fragments cross-sectional areas are much smaller than A_T.

The relative velocity between two objects can be found by using the rule of cosines [36]:

$$v_{rel}^2 = v_T^2 + v_F^2 - 2v_T v_F \cos\delta \tag{3.4}$$

v_T and v_F are the velocity moduli respectively of the target and the fragments, while δ is the angle between the two velocity vectors. The velocity of the fragments can be computed exploiting the hypothesis of quasi-circular orbits for the propagation of the debris cloud:

$$v_F \approx v_{circ} = \sqrt{\frac{\mu_E}{r}} \tag{3.5}$$

The angle δ can be found from the geometry of the problem. Considering the intersection of the fragments orbit and the target orbit depicted in Figure 3.2, $\cos\delta$ is obtained by applying the cosine rule to the green spherical triangle [18]:

$$\begin{aligned} \cos\delta &= \sin(\pi - i_F)\sin i_T \cos\Delta\Omega - \cos(\pi - i_F)\cos i_T = \\ &= \sin i_F \sin i_T \cos\Delta\Omega + \cos i_F \cos i_T \end{aligned} \tag{3.6}$$

with i_F inclination of the fragments orbit, i_T the inclination of the target orbit and $\Delta\Omega$ is the difference in RAAN between the two orbits. Note that applying the sine rule to the red spherical triangle in Figure 3.2, one obtains the same condition in Eq. 2.27. It is worth to point out that an intersection between the target and the fragment cloud is only possible if the target spends part of its orbit within the cloud. If $i_T > i_F$, the target covers a wider range in latitude with respect to the fragments, therefore there exist some values of argument of latitude of the target for which $\beta_T > \beta_F$, hence no intersection is geometrically possible. To compute the average relative velocity, the approach proposed in [18] is followed, where the orbits of the fragments are assumed to have the same inclination as the parent orbit.

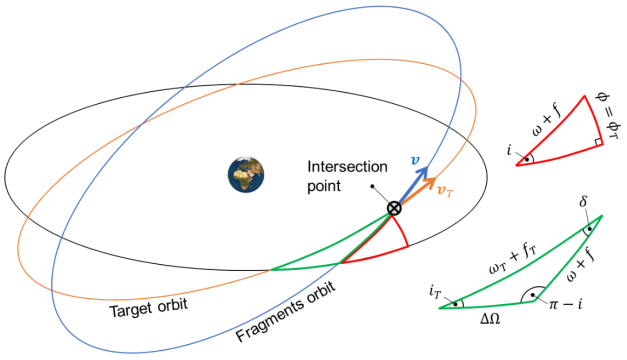

Figure 3.2: Spherical triangles due to the intersection between target and fragments orbit [18].

In the implementation of the computation of the collision velocity carried out by Letizia et al. [36], the average impact velocity was computed with the integral mean of the velocity function for $\Delta\Omega$ from 0 to 2π, that is:

$$\overline{v}_{rel} = \frac{1}{2\pi} \int_0^{2\pi} v_{rel}(\Delta\Omega)\, d\Delta\Omega. \tag{3.7}$$

This assumes that Ω is uniformly distributed among the fragments as a consequence of its randomisation and therefore that each $\Delta\Omega$ is equally probable. However, as explained by Giudici et al. [18], the averaging procedure should be done on the mean anomaly of the target $\overline{M}_T$ to take into account all possible conjunctions between target and fragments while the target moves on its fixed orbit. In particular, given a mean anomaly of the target $\overline{M}_T$, there exist two possible circular intersecting fragments orbit with a shift in RAAN. Therefore, the average impact velocity must be computed with respect to $\overline{M}_T$, which in turn can be cast as a function of the true anomaly f_T with a change of variables:

$$\frac{d\overline{M}_T}{df_T} = \frac{(1 - e_T^2)^{3/2}}{(1 + e_T \cos f_T)^2}. \tag{3.8}$$

Hence the average impact velocity becomes:

$$\overline{v}_{rel} = \frac{1}{2\pi} \int_0^{2\pi} \frac{1}{2} \sum_{j=1}^{2} v_{rel}\left(\Delta\Omega_j(f_T)\right) \frac{d\overline{M}_T}{df_T}\, df_T. \tag{3.9}$$

Notice that $\Delta\Omega_j$ are the two solutions to the cotangent law applied to the green spherical triangle in Figure 3.2:

$$\begin{aligned}\cos\Delta\Omega\cos i_T &= \cot u_T \sin\Delta\Omega - \sin i_T \cot(\pi - i_F) = \\ &= \cot u_T \sin\Delta\Omega + \sin i_T \cot(i_F)\end{aligned} \tag{3.10}$$

where $u_T = \omega_T + f_T$ is the argument of latitude of the target. Moreover, the velocity of the target v_T is dependent on the position of the target along its orbit, which in turn depends on the true anomaly of the target, hence v_T is variable within the integral. The correction in the computation of the average velocity implies significant differences in the velocity profile with respect to the previous model, as shown in [18].

Eq. 3.3 only holds for targets on circular orbits, for which the spatial density $N(r, \beta, t)$ is constant independently to the position of the target along its orbit. However, when dealing with elliptical orbits, this assumption is not valid anymore. Therefore, the impact rate must take into account the variation of spatial density with respect to the position of the target on its orbit, which depends on its mean anomaly [18]:

$$\bar{\dot{\eta}} = \frac{\sigma_c}{2\pi} \int_0^{2\pi} N\left(r_T(f_T), \beta_T(f_T)\right) \frac{1}{2} \sum_{j=1}^{2} v_{rel}\left(\Delta\Omega_j(f_T)\right) \frac{d\overline{M}_T}{df_T}\, df_T. \tag{3.11}$$

with β_T target latitude and r_T target position.

3.3. Collision probability results

The method developed throughout this Chapter has been applied to a reference scenario, to study the effect of a breakup on given targets and to understand how the characteristics of the targets affect the resulting collision probability. The considered breakup is the one of Cosmos 1867, whose evolution in time has already been studied in Section 2.6 considering fragments from 1 mm to 10 cm. The characteristics of the fragmentation are reported in Table 2.3. The impact rate and the collision probability have been computed for three targets, whose characteristics have been retrieved from [31] and can be found in Table 3.1.

Table 3.1: Characteristics of the targets.

	h_p [km]	h_a [km]	i [deg]	Mass [kg]	Size [m]
SC_1	816.0959	818.9741	98.73	4090	6.91
SC_2	818.5311	832.9389	98.83	2490	5.17
SC_3	1099.8350	1099.8350	63.00	1000	2.41

These three targets have been selected to assess the impact of their inclination and cross-sectional area on the resulting collision probability. The results of the impact rate and cumulative collision probability in time are shown in Figures 3.3 and 3.4.

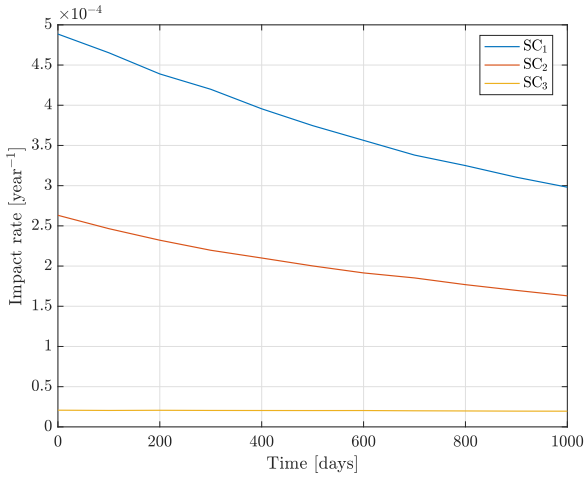

Figure 3.3: Impact rate in time.

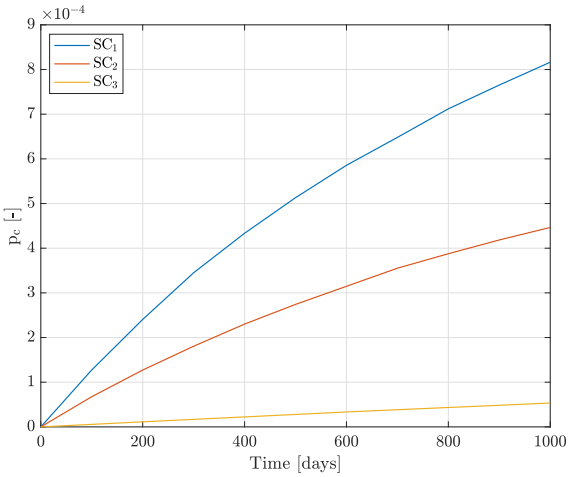

Figure 3.4: Collision probability in time.

The decrease of the impact rate in time is due to the reduction of the spatial density evaluated at r_T and β_T caused by atmospheric drag. As for the collision probability, it is evident that the first two spacecraft, which are at a higher inclination with respect to the one of the breakup, are more affected by the fragmentation, having a higher resulting collision probability than the third spacecraft, which instead is at a lower inclination. The effect of the cross-sectional area is also clear. In fact, considering that SC_1 and SC_2 are at a very similar inclination, the higher cross-sectional area of SC_1 causes a higher collision probability. Moreover, the impact rate with respect to time and the target position has been computed and plotted. The results are shown for SC_1 in Figure 3.5. As expected, since the inclination of the target orbit is higher than the inclination of the parent orbit, for some target positions no intersection - and therefore no impact - is possible.

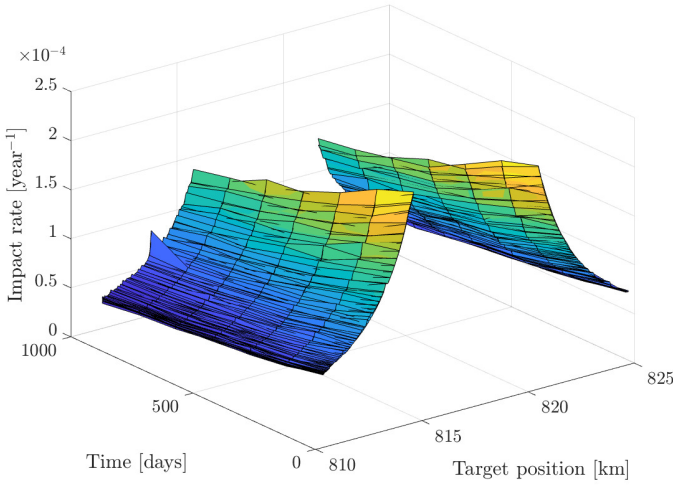

Figure 3.5: Impact rate with respect to spacecraft 1 position and time.

4 | Effect maps

This Chapter addresses the study of the impact of fragmentation events in terms of risks to other objects in orbit at various altitudes and inclinations in the LEO region. The collision probability computation model described in Chapter 3 is used to generate maps indicating the severity of the breakups. The lifetime of a debris cloud is also taken into account in the generation of the maps.

4.1. Adopted formulation

The limited computational effort of the continuum approach developed thus far allows the simulation of numerous possible breakup scenarios. This is exploited to carry out an analysis on the effects of breakups at several altitudes and inclinations on a set of target objects representing the active satellites in LEO [38]. As motivated by Letizia et al. [40], the long-term evolution of the debris environment is highly affected by fragmentation of large objects (for example, in the case of the Fengyun-1C fragmentation), hence the consequences of such breakups must be investigated. A possible approach consists in measuring the severity of these events by looking at the increase in the collision risk for operational satellites [40] and at the effects on the operational aspects of the debris environment, e.g. close conjunction alerts, therefore connecting the effects on operational satellites to the cost to operators. Moreover, the collision risk deriving from the breakups could be used as an indicator of the future availability of access to space [40].
In this thesis, the effects of potential breakups are studied with the first formulation of the Environmental Consequences of Orbital Breakups (ECOB) index proposed by Letizia et al. [38]. This formulation of ECOB is a severity index since it only represents the risk posed by breakups to other objects in orbit without considering the likelihood of the fragmentation. This approach requires two steps: the definition of a set of *reference targets*, representative of the entire population of active satellites, and the actual evaluation of the index in a pre-defined grid in semi-major axis and inclination. A virtual breakup is generated in each bin of the predefined semi-major axis-inclination grid with the NASA Standard Breakup Model, the fragment cloud is propagated with the continuum approach

detailed in Chapter 2 and the cumulative collision probability between fragments and the reference targets is computed according to Eq. 3.1. The timespan for the cumulative collision probability computation has been chosen as 15 years as already done in [41] to represent the average duration of a space mission. The final value of the ECOB index is computed as:

$$e = \frac{1}{A_{tot}} \sum_{j=1}^{N_t} p_c(t)_j A_j \tag{4.1}$$

where e is the value of the index, also indicated as *effect* of collisions or explosions, A_{tot} is the total cross-section of all the representative targets in m^2, N_t is the number of targets, $p_c(t)_j$ the collision probability computed for each target j and A_j is the cumulative cross-section in m^2 of the objects of the j-th bin. The ratio $\frac{A_j}{A_{tot}}$ can be seen as a weighting factor taking into account that each cell of the grid represents a different share of the total cross-sectional area [38].

Since the focus of this analysis is the LEO region, the grid used for the generation of the effect maps is defined in semi-major axis and inclination, respectively, between 400 km and 1600 km with a step of 25 km and between 0° and 180° with a 5° step. It is important to stress that this grid extends beyond the limits of applicability of the continuum approach developed in Chapter 2, as for the generation of the maps the method has been applied below 700 km and above 1000 km. For higher altitudes, the effect of SRP and third-body (3B) perturbation should be included in the model for more accurate results, while below 700 km the drag effect is underestimated. Despite the resulting lower accuracy of the maps in those regions, the effect maps are expected to capture the most affected regions when fragmentations occur.

For the evaluation of the consequences of in-orbit fragmentations, three sets of representative targets have been provided. The characteristics of the operational spacecraft are retrieved from ESA DISCOS Database [49]. A grid in semi-major axis and inclination is used for the characterisation of the operational spacecraft. The cumulative cross-sectional area $\sum A_c$ is computed for each bin of the grid and a representative target is identified in the cells containing the highest $\sum A_c$ [38], which represent the regions most susceptible to breakups. The three lists of targets used in this analysis are representative of the active satellites in LEO in 2017, in 2023 without the Starlink constellation and in 2023 with the Starlink constellation. These representative targets are characterised by their Keplerian elements, the average area (i.e. the cumulative cross section of the objects of that bin)

and the total area. Their total area with respect to the semi-major axis-inclination grid is shown in Figure 4.1a, Figure 4.1b and Figure 4.1c.

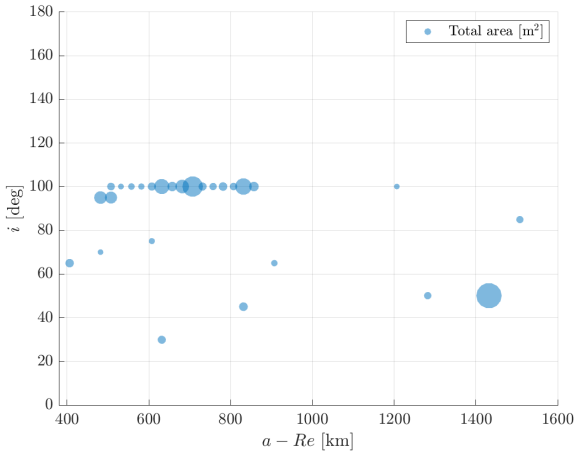

(a) 2017.

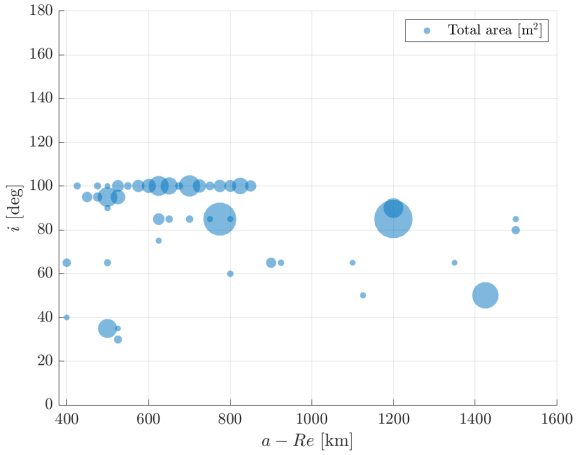

(b) 2023.

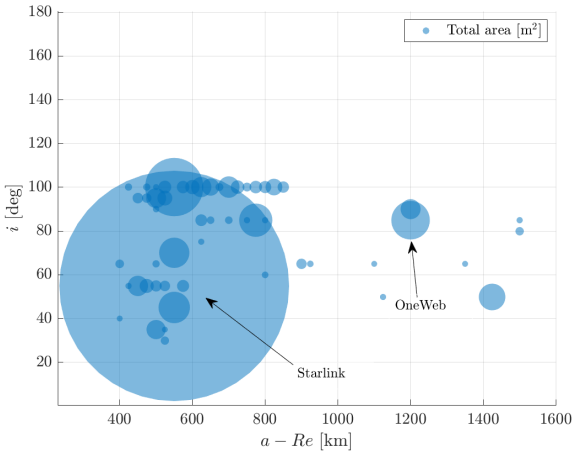

(c) 2023 with Starlink.

Figure 4.1: LEO region representative targets in semi-major axis and inclination grid in 2017 (a), 2023 (b) and 2023 including Starlink (c).

Currently, SpaceX has launched the largest number of satellites for a constellation, with Starlink. It consists of over 5000 small satellites with a mass of 260 kg, although the company has planned the launch of 12000 satellites, with possible increases. The majority of Starlink's satellites are placed on quasi-circular orbits at 550 km of altitude and 53° of inclination [45]. Given the vast number of satellites of this megaconstellation, it is important to monitor its impact on the LEO environment. Therefore, it is of interest to carry out an analysis on the variations of the effect when adding Starlink's contribution to the representative targets.

For all scenarios, two types of evaluations are made:

- Effect maps over a timespan of 15 years, with a fixed time step Δt equal to 200 days for the evaluation of the collision probability.
- Effect maps with a variable Δt related to the lifetime of debris clouds, varying with the value of semi-major axis.

4.1.1. Lifetime of a debris cloud

One of the main novelties of this work consists in computing the effect maps with a variable time step for the evaluation of the cumulative collision probability, taking into account the lifetime of the debris cloud generated in each bin of the semi-major axis and inclination grid. This approach offers a more accurate representation of the effect of breakups with respect to maps with a fixed time step, specifically for breakups occurring at low altitudes. When considering a fixed value for the time step Δt, if the lifetime of the cloud is lower than the time step, the effect of the debris cloud is evaluated only at one instant, while at the next the debris cloud has re-entered and does not have any significant effect. For this reason, it is useful to define a step according to the lifetime of the cloud generated in each bin.
The lifetime of a debris cloud depends on the lifetime of all its fragments. Therefore, the lifetime of the cloud is computed here as the average of the lifetimes of its fragments. This is motivated by the fact that in the continuum approach fragments down to millimitre size are considered, which can reach high altitudes with respect to the location of the breakup after the fragmentation event. As a consequence, they have long lifetimes. Considering the average of the lifetimes of the fragments therefore averages out this effect, allowing a more realistic lifetime computation for the cloud.

The value of the lifetime (τ_L) for each fragment is computed according to the King-Hele's formulation [30]. Some useful parameters are defined first:

$$\delta = \frac{c_d A}{M}, \quad x = ae, \quad \beta = \frac{1}{H} \tag{4.2}$$

where δ is the effective area-to-mass ratio already defined in Section 2.2.3. The expression for τ_L depends on the semi-major axis a and on the value of eccentricity e, divided into three ranges:

- $0 < e < 0.02$

$$\begin{aligned} \dot{T} &= -3\pi\delta a\rho_{ref}\exp(-z)[I_0(z) + 2eI_1(z)] \\ \tau_L &= -\left(\frac{3eT}{4\dot{T}}\right)\frac{I_0(z)}{I_1(z)}\left[1 + 2e\frac{I_1(z)}{I_0(z)} - \frac{9}{40}ez + \frac{H}{2a}\right] \end{aligned} \tag{4.3}$$

- $0.02 < e < 0.2$

$$\begin{aligned} B &= \frac{2\pi}{T}\delta\rho_{ref}xI_1(\beta x)\exp(-\beta x - e) \\ \tau_L &= \frac{e^2}{2B}\left(1 - \frac{11}{6}e + \frac{29}{16}e^2 + \frac{7H}{8a}\right) \end{aligned} \tag{4.4}$$

- $0.2 \leq e < 1$

$$\begin{aligned} \dot{T} &= -3\delta\rho_{ref}\left(\frac{\pi Ha}{2e}\right)^{1/2}\frac{(1+e)^{3/2}}{(1-e)^{1/2}}\left[1 - \frac{8e - 3e^2 - 1}{8z(1-e)^2}\right] \\ f(e) &= \frac{3+e}{(1+e)\sqrt{1-e}} - 3 - \frac{1}{\sqrt{2}}\ln\frac{\sqrt{2} + \sqrt{1-e}}{(\sqrt{2}+1)\sqrt{1+e}} \\ F(e) &= \frac{3(1-e)^{1/2}(1+e)^2}{8e^2}f(e)\left[1 - \frac{H(8e - 3e^2 - 1)}{8r_p e(1+e)}\right] \\ \tau_L &= -\frac{eT}{\dot{T}}F(e) \end{aligned} \tag{4.5}$$

where T is the period of the orbit, r_p the radius of pericentre of the orbit of the fragment, H the scale height, ρ_{ref} is the reference density value at the altitude of the fragment. H and ρ_{ref} are taken from Vallado [69] as in Section 2.2.3. I_k is the modified Bessel function of the first kind and order k (Eq. 2.19).

The results of the computation of the lifetime of a cloud generated from a catastrophic collision for each semi-major axis value a are represented in Figure 4.2a. As expected, the lifetime exhibits a quasi-exponential behaviour. With a 25 km step for the semi-major axis in the grid, the lifetime of the cloud exceeds 15 years - and therefore the time of the propagation for the computation of the effect maps - at 755 km of altitude.

Then, the time step Δt is determined according to the value of the lifetime. Two cases must be accounted for:

- If the lifetime of the cloud exceeds 15 years, then Δt is set to 1 year.
- If the lifetime of the cloud is less than 15 years, then a proportion is used to scale the time step with respect to the lifetime and to the overall propagation time:

$$\Delta t(a) = \frac{\tau_L(a)}{15[\text{years}]}365[\text{days}]. \tag{4.6}$$

Figure 4.2b shows the variation of Δt with respect to the semi-major axis.

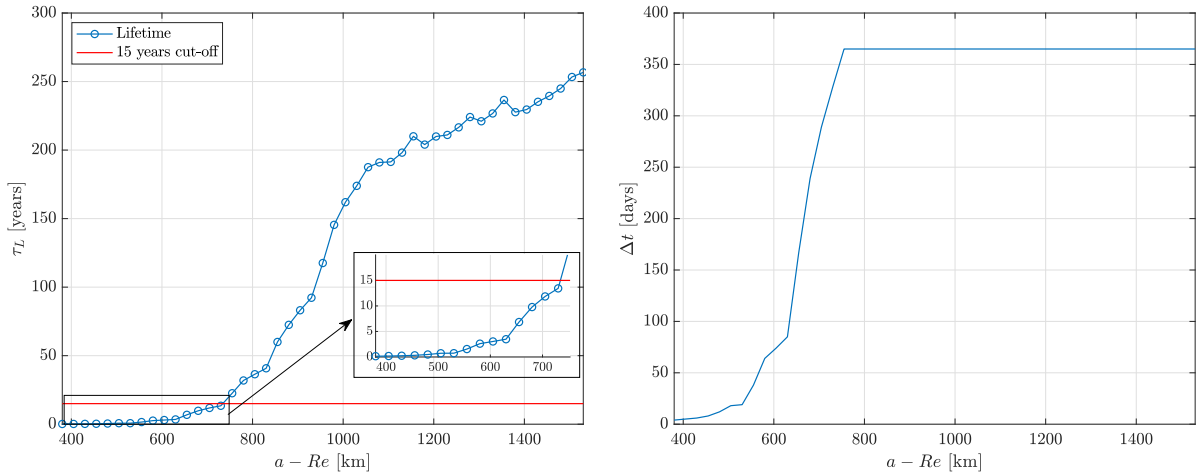

(a) Lifetime with respect to semi-major axis.

(b) Δt with respect to semi-major axis

Figure 4.2: Analysis of the lifetime of a debris cloud with respect to its altitude (a) and variation of the time step with altitude (b).

Since the Δt associated to the lowest semi-major axis values is small with respect to the 15 years of propagation, the computational effort required for the full propagation is very demanding. For this reason, an analysis is carried out to evaluate whether the propagation can be stopped earlier for debris clouds with a lifetime lower than 15 years. The number of debris in orbit over time starting from the time of band formation is monitored (Figure 4.3a). Then, the number of fragments still in orbit after a period equal to the lifetime of the cloud is computed for each cloud generated at various altitudes. In this work, a cloud is considered re-entered if the number of fragments in orbit does not exceed 5% with respect to the total number of fragments of the cloud at the beginning of the propagation. The results of this analysis are shown in Figure 4.3b, where the remaining percentage of fragments of debris clouds generated from catastrophic collisions at various semi-major axis values at the end of their respective lifetimes are represented.

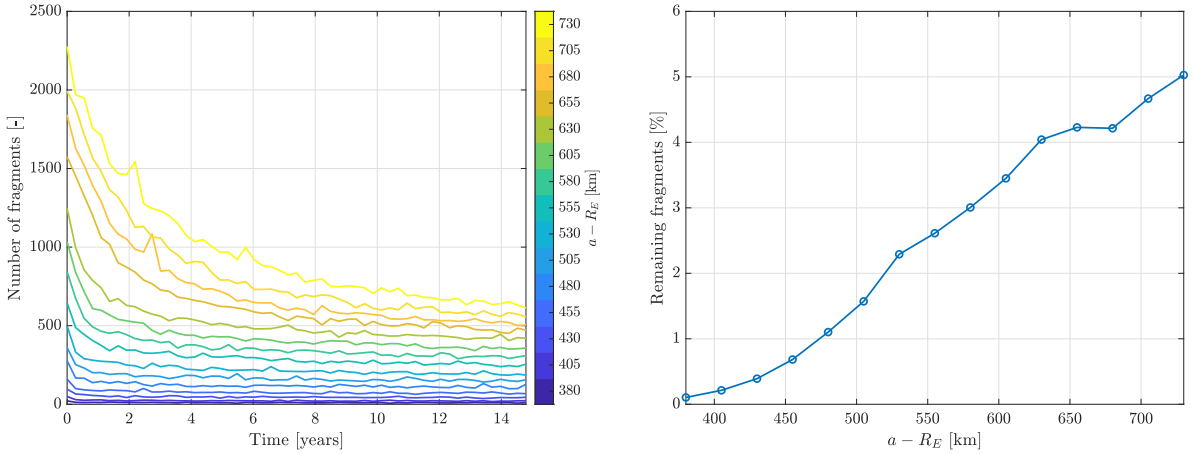

(a) Fragments in time.

(b) Remaining fragments.

Figure 4.3: Analysis on the evolution of fragments in orbit in time (a) and remaining fragments after the lifetime of the cloud (b) at various altitudes.

The results obtained from this analysis indicate that the clouds can be considered as re-entered after their lifetime, hence they can be propagated for a time equal to their lifetime, as it would be pointless to keep propagating them for 15 years. Therefore, the maps taking into account the lifetime of the cloud have both the propagation time and the time step varying with the altitude of the fragmentation.

4.1.2. Scenario 1 - Catastrophic collision

The first scenario to be analysed is the case of catastrophic collisions, which serves also as validation of the model. The breakups generated with the NASA Standard Breakup model in each cell of the semi-major axis-inclination grid are obtained with a fixed reference mass of 1000 kg. This is motivated by the correlation between the value of the fragmenting mass and of the index, which follows a power law [40]. Hence, once the effect maps for a fixed mass have been obtained, it is sufficient to rescale them to derive the results for a different fragmenting mass. Moreover, the collision velocity is set to 10 km/s for all fragmentations as already done by Letizia et al. [38], as it represents an average value in LEO. The generated fragments have a lower size limit of 1 cm. This choice is due to the fact that, if fragments down to 1 mm were considered, more than 2.4 million debris would be generated with the catastrophic collision resulting in a cumbersome analysis. All the effect maps generated in this Chapter are obtained by neglecting the phase of band formation and considering RAAN, argument of pericentre and mean anomaly of the fragments as already randomised after the breakup so as to allow the comparisons with

the maps obtained with the THEMIS software [7], where the same assumption has been made. It is important to point out that all the results shown in this Chapter are obtained using as total reference area A_{tot} in Eq. 4.1 the total cross-sectional area of the targets in 2017. This is due to the fact that the term A_{tot} is only a scaling factor, therefore using the same reference area for all three reference target lists allows to compare the maps obtained in the three cases, highlighting the effect of adding representative targets in 2023 and the effect of Starlink with respect to the population without the constellation. The results obtained for the target lists in 2017, 2023 and 2023 adding the Starlink constellation for a fixed Δt are shown in Figures 4.4a, 4.4b, 4.4c respectively.

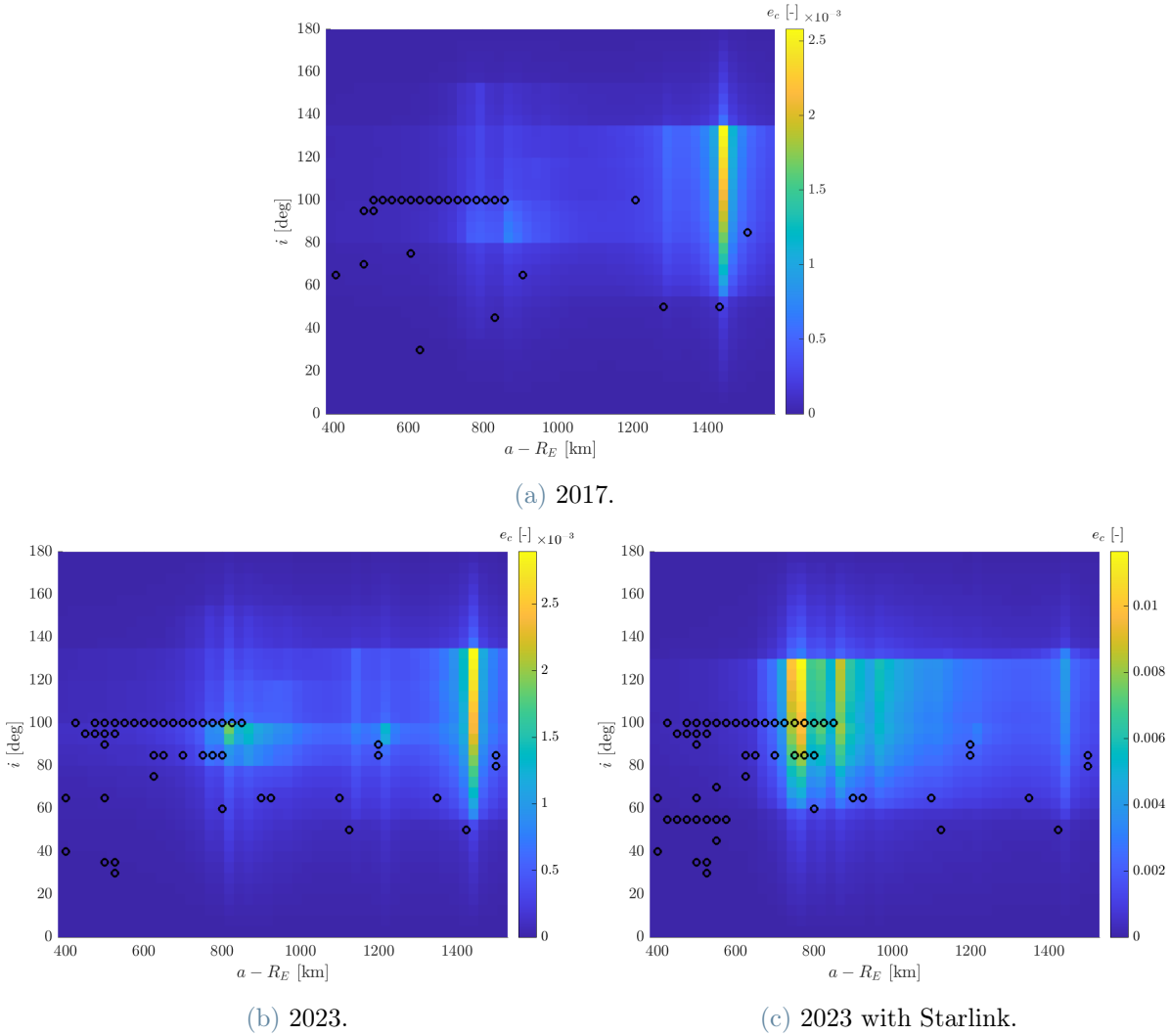

(a) 2017.

(b) 2023.

(c) 2023 with Starlink.

Figure 4.4: Effect maps of catastrophic collisions with targets of 2017 (a), 2023 (b) and 2023 with Starlink constellation (c), with a fixed Δt. Fragments lower size 1 cm.

The effect map for targets in 2023, without the Starlink constellation (Figure 4.4b) can

be used to validate the maps obtained with the analytical method by comparison with the effect maps derived with THEMIS in [7], taken as reference. It is worth to mention that THEMIS is able to produce the maps with the extended formulation of the ECOB index, taking into account also the likelihood of the breakups. However, for this comparison, only the maps referred to the effect - hence, the severity of the breakup - are considered. The map obtained with the analytical method presents similar features to the reference one (Figure 4.5). Specifically, it is able to capture the same order of magnitude in the effect and the same concentration of the effect in the altitude region around 800 km, with the peak at 90°, and slightly above 1400 km, with the peak at 130°. The differences in the maps may be due to the fact that the maps in this thesis are obtained with the extension of the analytical approach beyond the regions for which it has been validated, respectively, below 700 km and above 1000 km, making the evolution of the spatial density less reliable. Moreover, the intrinsic accuracy of Starling, used within THEMIS, is bound to produce more precise results. Nonetheless, the maps derived in this work are deemed as sufficiently precise since they are able to grasp the fundamental features of the THEMIS ones, in much less time. On top of this, the maps obtained with the analytical method show the same difference with respect to the previous effect maps generated with the CiELO software presented in [40] already demonstrated by the maps obtained with THEMIS. In fact, the correction in the collision probability computation applied in this work causes the maps to lose the symmetry in inclination of the peaks of the effect.

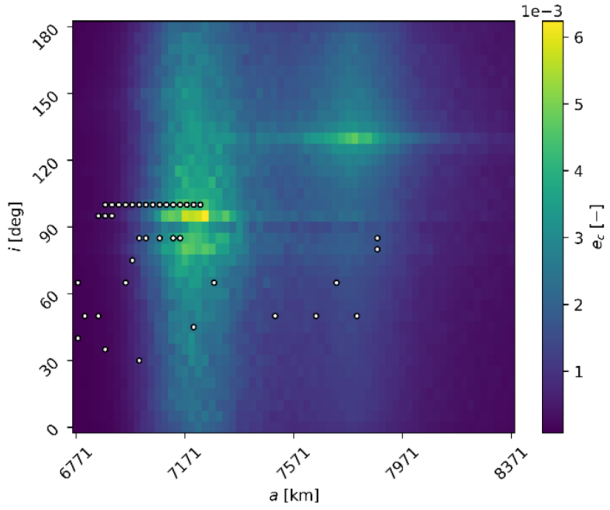

Figure 4.5: Effect map obtained with the THEMIS software for catastrophic collisions with 2023 targets without constellations, from [7].

The effect maps allow to determine the consequences of the increase of satellites in orbit throughout time, by looking at the differences among the maps in 2017 (Figure 4.4a),

2023 (Figure 4.4b), and 2023 with the addition of Starlink (Figure 4.4c). It is evident that the increase of representative targets in 2023 with respect to 2017 (predominantly at low altitudes) has caused a growth in the effect of catastrophic collisions, especially around 800 km of altitude. The addition of the Starlink constellation among the representative targets has an even greater consequence on the effect map. The effect increases of up to one order of magnitude and the most significant repercussions of Starlink can be found between 800 and 1000 km. This is due to the fact that the breakups occurring at lower altitudes re-enter the atmosphere faster than those at higher altitudes, whose fragments decay throughout the 15 years of propagation under the effect of drag, therefore running into Starlink and increasing the collision probability. It is also important to note that the peak of the effect can be seen at around 125°, which is to be expected since the majority of Starlink representative targets has an inclination of 55°. This is due to the fact that the maximum relative velocity is found for the condition $\sin(i_F) = \sin(i_T)$, when $i_T < 90°$ and $i_F = \pi - i_T$ hence leading to a shift in the inclination of the maximum effect with respect to the inclination of the targets.
The same maps have been generated also with a variable Δt, for the same sets of targets. The results are shown in Figures 4.6a, 4.6b and 4.6c.

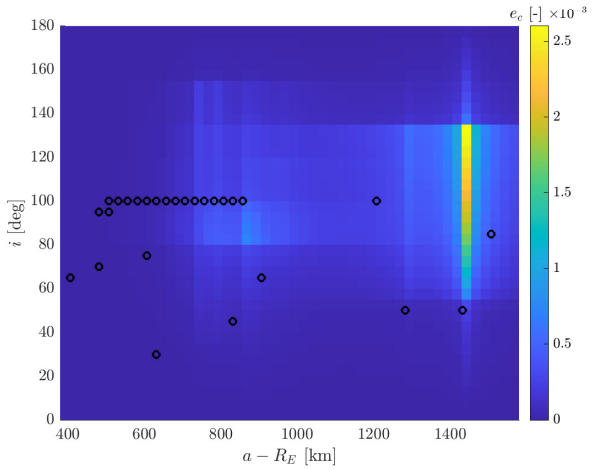

(a) 2017.

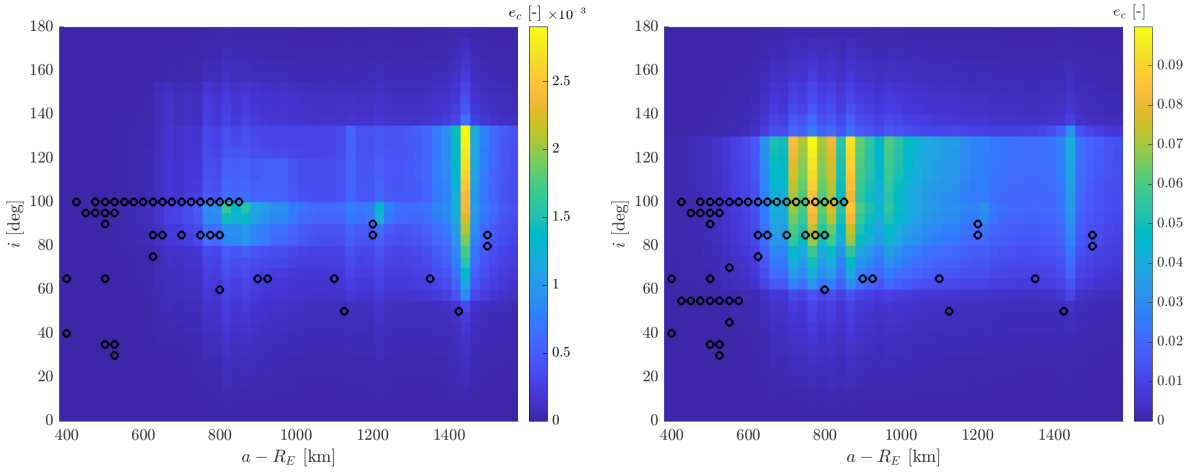

(b) 2023.

(c) 2023 with Starlink.

Figure 4.6: Effect maps of catastrophic collisions with targets of 2017 (a), 2023 (b) and 2023 with Starlink constellation (c), with a variable Δt. Fragments lower size 1 cm.

The results show that no significant change can be found in the effect maps for the representative targets of 2017 (Figure 4.6a) and 2023 without Starlink (Figure 4.6b). Conversely, the effect map considering Starlink (Figure 4.6c) presents significant changes. This is more visible when looking at the details of the maps at low altitudes with a fixed Δt and a variable one, respectively in Figures 4.7a and 4.7b. This difference can be explained in the fact that the variable Δt allows a more accurate representation of the consequences of breakups at low altitudes, where Starlink's representative targets reside. Using a variable Δt leads to a higher absolute value of the effect. Moreover, higher values of the effect can be found at lower altitudes with respect to Figure 4.4c, reaching almost 600 km. Indeed, using a time step smaller than the 200-day fixed one allows to better capture the consequences of breakups occurring at low altitudes despite their short lifetimes.

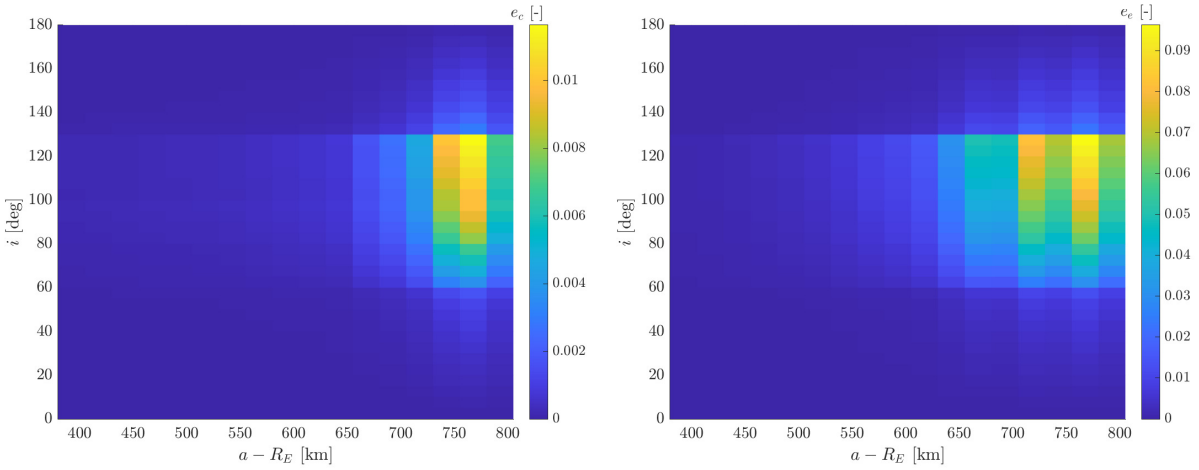

(a) Fixed Δt. (b) Variable Δt.

Figure 4.7: Details of the effect maps at low altitudes when considering a fixed Δt (a) and a variable Δt (b).

4.1.3. Scenario 2 - Non-catastrophic collision

In this second scenario, the effect of non-catastrophic collisions is analysed. The reference mass for the generation of the breakups is set at 1000 kg again and the relative impact velocity is 1 km/s. The lower size limit for the fragments is set to 1 mm since the number of debris generated by a non-catastrophic collision is lower than that of catastrophic collisions, hence the computational burden is reduced. The results for the maps with a fixed Δt are shown in Figures 4.8a, 4.8b, 4.8c.

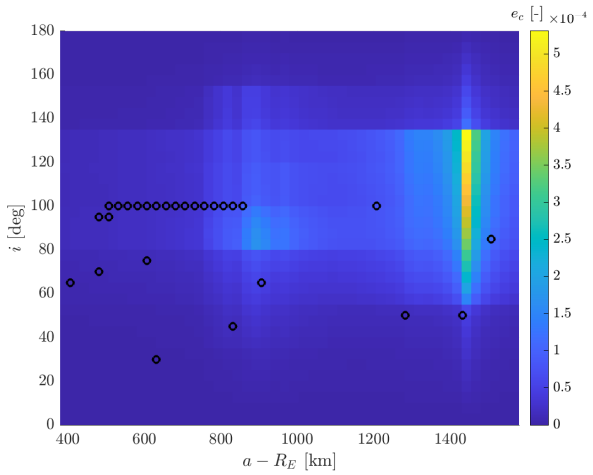

(a) 2017.

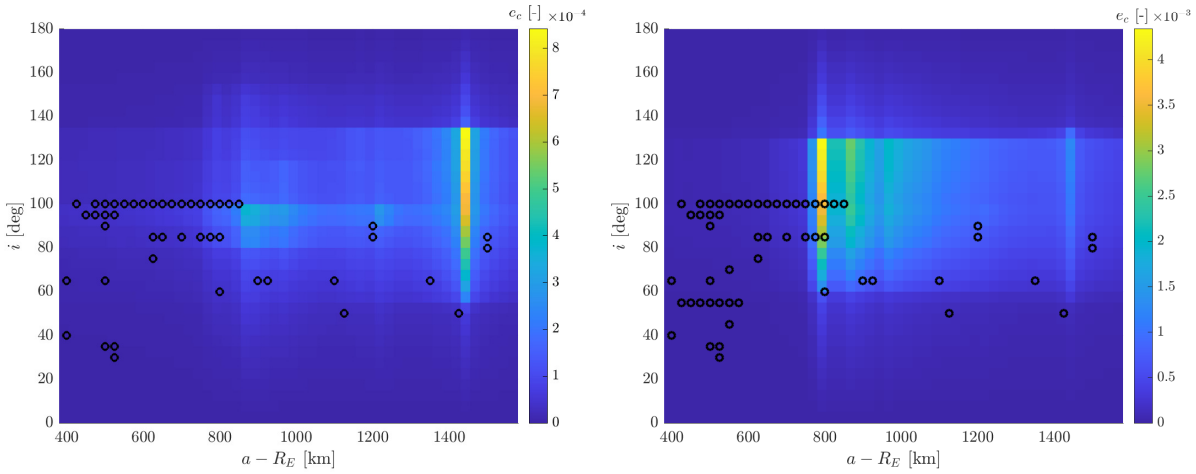

(b) 2023.

(c) 2023 with Starlink.

Figure 4.8: Effect maps of non-catastrophic collisions with targets of 2017 (a), 2023 (b) and 2023 with Starlink constellation (c), with a fixed Δt. Fragments lower size 1 mm.

The main difference between the catastrophic and non-catastrophic cases is that in the latter scenario, the produced effect is less relevant as it is one order of magnitude lower than for catastrophic collisions. This is to be expected because of the lower number of fragments produced by non-catastrophic collisions and of the lower velocity imparted to them. The same trends in the effect maps can be found, although less pronounced. Again, there is an increase in the value of the effect when going from 2017 (Figure 4.8a) to 2023 (Figure 4.8b), especially around 800 to 1000 km, and a more significant effect is seen when adding Starlink's representative targets (Figure 4.8c), with an increase of one order of magnitude, mainly around 800 to 1000 km, with a peak at 125°. Notice that the fact that catastrophic collisions fragments spread more than the non-catastrophic ones is not captured in these maps because of the different fragments size ranges used for the maps.

The same analysis has been carried out with a variable Δt. The generated maps can be found in Figures 4.9a, 4.9b and 4.9c.

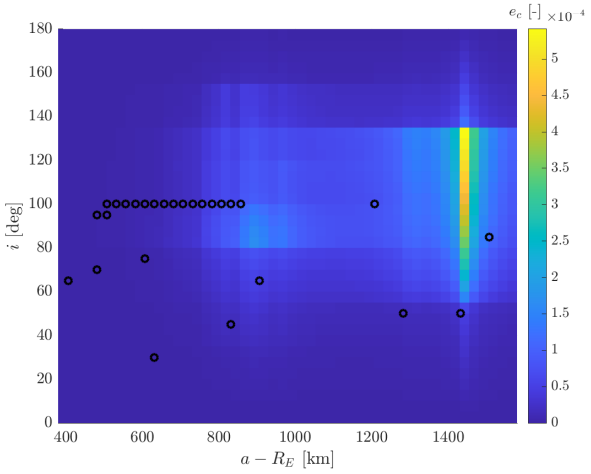

(a) 2017.

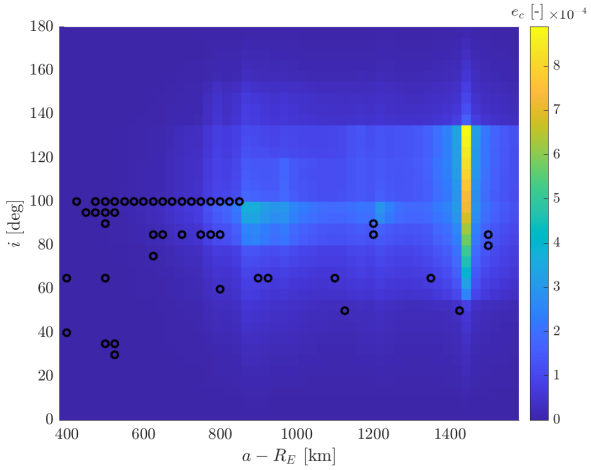

(b) 2023.

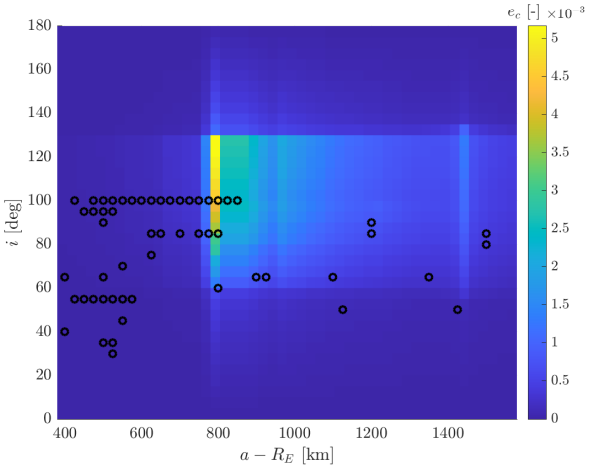

(c) 2023 with Starlink.

Figure 4.9: Effect maps of non-catastrophic collisions with targets of 2017 (a), 2023 (b) and 2023 with Starlink constellation (c), with a variable Δt. Fragments lower size 1 mm.

This analysis exhibits the same behaviour as the case of catastrophic collisions as well. There are no significant differences between the maps of 2017 and 2023 with a fixed and variable Δt, while the map including Starlink (Figure 4.9c) presents a higher value of the effect, which spreads towards lower altitudes with respect to the case of fixed Δt (Figure 4.8c).

4.1.4. Scenario 3 - Explosion

The last scenario is the case of the explosion of rocket-bodies. Here, the lower size limit for fragments has been set to 5 mm and the reference mass is 1000 kg. The results for the maps with a fixed Δt are shown in Figures 4.10a, 4.10b, 4.10c.

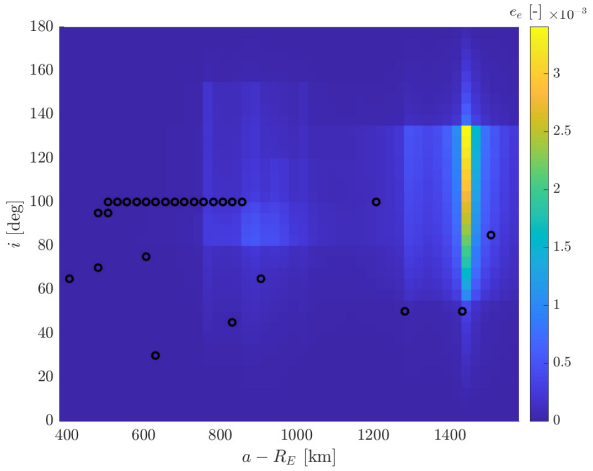

(a) 2017.

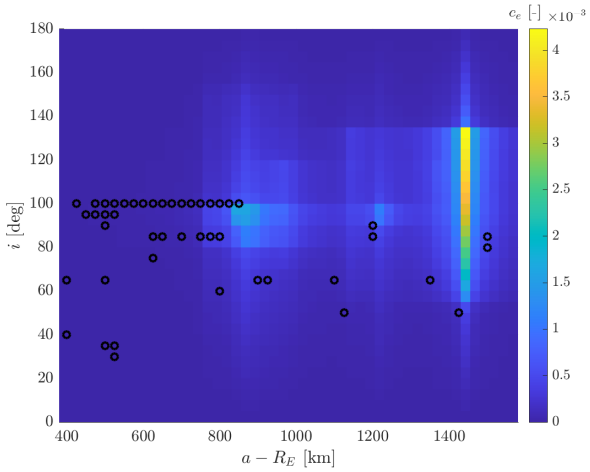

(b) 2023.

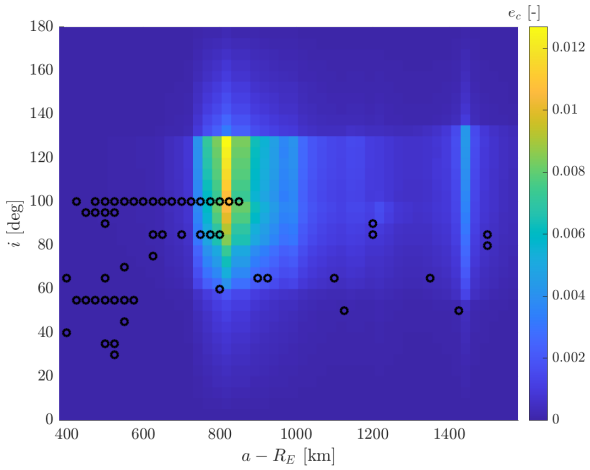

(c) 2023 with Starlink.

Figure 4.10: Effect maps with targets of 2017 (a), 2023 (b) and 2023 with Starlink constellation (c), with a fixed Δt for rocket-body explosions. Fragments lower size 5 mm.

The same trend visible in the previous cases can be seen for explosions as well. The effect of collisions is more pronounced when considering targets in 2023 with respect to 2017, especially around 800 km of altitude. The addition of Starlink significantly impacts the maps, increasing the effect of one order of magnitude. When Starlink is present (Figure 4.10c), fragmentations occurring at around 800-1000 km of altitude are particularly dangerous, as the fragments decaying throughout time intersect the Starlink satellites at low altitude. The confirmation that the increase of the effect is due to Starlink can be found in the inclination of the peak of the effect, which is around 125°.
The same maps obtained with a variable Δt are shown in Figures 4.11a, 4.11b and 4.11c.

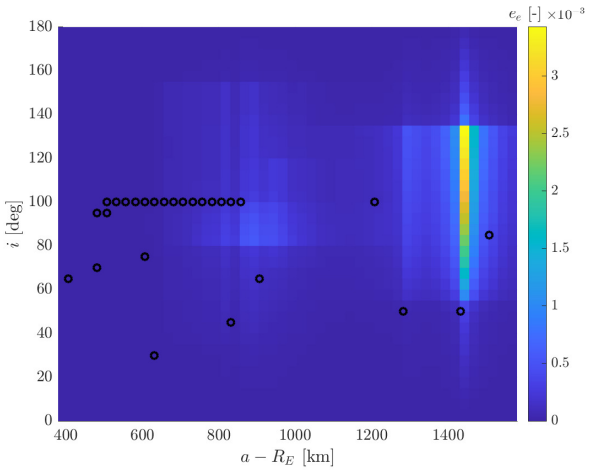

(a) 2017.

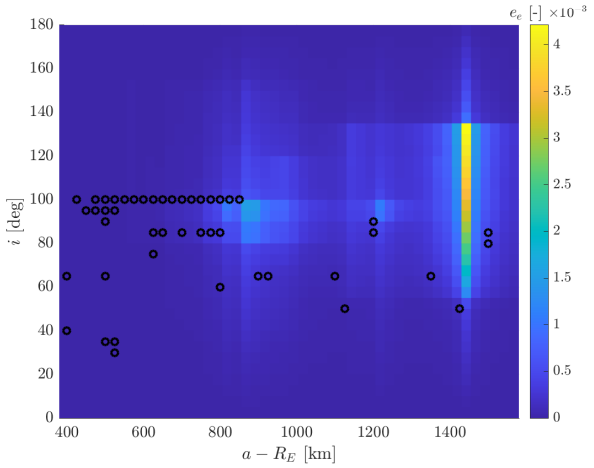

(b) 2023.

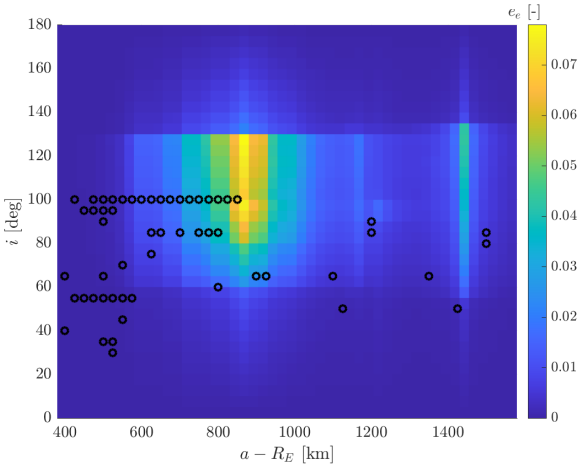

(c) 2023 with Starlink.

Figure 4.11: Effect maps with targets of 2017 (a), 2023 (b) and 2023 with Starlink constellation (c), with a variable Δt for rocket-body explosions. Fragments are considered down to 5 mm size.

As in the previous cases, the effect maps for targets in 2017 and 2023 without Starlink are not much affected by the change in Δt, while in the Starlink case (Figure 4.11c) the effect maps undergo significant changes. The variable Δt allows to better characterise fragmentations at low altitudes, hence the value of the effect increases and the effect is spread towards lower altitudes. Fragmentations occurring as low as at 600 km now exhibit a significant effect.

5 | Conclusions and future developments

5.1. Summary

Space debris have become a persistent issue and a growing threat to operational satellites around the Earth. As such, it is important to be able to model the evolution of debris clouds and the consequences of breakups on satellites to avoid catastrophic events and ensure a more sustainable exploitation of space.

The aim of this thesis was the development of a continuum approach to model debris clouds and to assess the collision probability of target spacecraft with the fragments. In the first part of the thesis, the long-term evolution of debris clouds has been tackled. Fragmentation events have been modelled with the NASA Standard Breakup Model, according to the nature of the event (collision or explosion). Then, the cloud evolution was studied through the continuity equation, monitoring the change of the spatial density of the debris cloud in time, modelled with respect to the radial distance and extended to account for the latitude. This approach is able to include in the formulation millimitre-sized fragments, which is one of its advantages with respect to classical semi-deterministic approaches where the trajectories of individual fragments are propagated. To increase the accuracy of the method, it has been found that subdividing the fragments into bins according to their area-to-mass ratio either by using the same number of fragments in each bin or logarithmically spaced bins provides the best results. This approach was able to provide accurate results in reduced computational time.

The method implemented by Letizia et al. [36] for the computation of the collision probability between target spacecraft and the fragments of a debris cloud has been improved with the correction of a previous error, applying the work of Giudici et al. [18] to the formulation developed in this thesis. This has allowed to correctly assess the collision probability deriving from breakups and how the characteristics of the targets, such as the inclination and cross-sectional area, affect it.

The final application of the method developed throughout the thesis is the generation of

effect maps, to evaluate the severity of breakups occurring at several altitudes and inclinations in the LEO region. This was carried out by using the formulation of the effect term of the ECOB index [39]. The resulting maps show the impact of the fragmentations on pre-defined sets of representative targets, highlighting the most dangerous regions for operational satellites and the detrimental effect of megaconstellations. The effect maps are compared with the ones obtained with the THEMIS software [7] to assess their validity. The maps generated with the continuum approach are able to grasp the main features of the THEMIS maps, despite the extension of the continuum method beyond its validity limits, giving reliable results in a reduced computational time. A novelty is introduced in the computation of the maps to better characterise the effect of breakups occurring at low altitudes, by using a variable time step for the computation of the collision probability, varying with the value of semi-major axis according to the lifetime of debris clouds. The results show that the severity of breakups increases with the growing number of operational satellites in time. This is particularly evident when constellations such as Starlink are included in the target sets, making the consequences of breakups more severe. The maps indicate that the breakups occurring between 800 km and 1000 km of altitudes and slighlty above 1400 km produce the most critical effect.

5.2. Limitations and future work

This last section is dedicated to the limitations of the work and further advances for future developments. The main limitations of this thesis are summarised hereafter:

- Limited application: this approach is only applicable in LEO, because of the assumptions employed in the model (the most relevant one being quasi-circular orbits).
- Perturbation modelling: this method is able to include the effect of the Earth's oblateness only in the short period, while the effect of drag is propagated in the long period as well. The continuum model considers drag as the only perturbation, hence it is applicable only after band formation, when the Earth's oblateness is negligible. Moreover, this approach has been validated only for altitudes between 700 km and 1000 km. Indeed, below 700 km the effect of drag is underestimated, while above 1000 km the effect of SRP and third-body perturbation should be included for more precise results.
- Propagation: the method of characteristics has been used to reduce the PDE into a set of ODE. The analytical solution is then found only along the characteristic lines.

- Source/sinks terms: throughout this work, the source and sinks terms of the continuity equation have been considered null. However, secondary phenomena should be accounted for to obtain more precise results.
- Severity maps: the maps generated in this work are effect maps, hence they only account for the severity of the breakups, neglecting their likelihood.

Future work should aim at overcoming these limitations. In particular, the effect maps should be generated with this model of the continuum approach, extending its validity for instance with the finite difference scheme [32]. This was already done in [39], however the computation of the collision probability was still affected by the error corrected in this thesis. Implementing the corrected version with the extended validity with this model would allow to maintain a low computational effort with respect to the one required by the THEMIS software, while improving the accuracy of the generated maps, for preliminary analyses. The limitations in terms of applications can also be overcome with a multi-dimensional formulation of the continuum approach, which has already been carried out with the Starling suite by Frey et al. [16], further improved by the work of Giudici et al. [19] and then used for the generation of very precise effect maps with the THEMIS software. This also allows to extend the model to other orbital regions and it applies an interpolation scheme to the characteristics.
Moreover, the aim of the continuum approach developed in this thesis is to build a model capable of simulating the long-term evolution of debris clouds in LEO. To this aim, possible secondary phenomena to account for with the source and sinks term include the launch traffic model developed in [3] and the feedback effect formulated in [9]. This would give a more precise insight on the effect of breakups on the LEO population.
As for the assessment of the consequences of breakups, further development of this work should apply the developed continuum model to compute the full ECOB index, considering also the likelihood of the breakups, as well as the evaluation of the index throughout different mission profiles to account for disposal strategies. This would allow carry out a comparison with the complete maps generated with THEMIS and provide preliminary results for the full index in a reduced time. These maps could then be applied to analyse the impact of potential space missions on the debris environment.

Bibliography

[1] L. Anselmo and C. Pardini. Ranking upper stages in low earth orbit for active removal. *Acta Astronautica*, 122, 2016. ISSN 00945765. doi: 10.1016/j.actaastro.2016.01.019.

[2] J. Ashenberg. Formulas for the phase characteristics in the problem of low-earth-orbital debris. *Journal of Spacecraft and Rockets*, 31, 1994. ISSN 00224650. doi: 10.2514/3.26556.

[3] J. Carlos and V. Escobar. Continuum approach for the modelling of debris population and launch traffic in low earth orbit. 2022.

[4] C. Colombo. Planetary orbital dynamics (planodyn) suite for long term propagation in pertubed environment. In *Proceedings of the 6th International Conference on Astrodynamics Tools and Techniques (ICATT)*, 2016.

[5] C. Colombo, F. Letizia, and H. G. Lewis. Spatial density approach for modelling of the space debris population. *Advances in the Astronautical Sciences*, 158, 2016. ISSN 00653438.

[6] C. Colombo, M. Trisolini, A. Muciaccia, L. Giudici, J. L. Gonzalo, S. Frey, B. D. Campo, F. Letizia, and S. Lemmens. Evaluation of the space capacity share used by a mission, 2022.

[7] C. Colombo, A. Muciaccia, L. Giudici, J. L. Gonzalo, A. Masat, M. Trisolini, B. D. Campo, F. Letizia, and S. Lemmens. Tracking the health of the space debris environment with themis. *Aerospace Europe Conference 2023 – 10th EUCASS – 9th CEAS*, 2023. doi: 10.13009/EUCASS2023-060.

[8] H. D. Curtis. *Orbital Mechanics for Engineering Students*. 2013. doi: 10.1016/C2011-0-69685-1.

[9] C. Duran, L. Giudici, and C. Colombo. Modelling the whole space debris environment through a spatial density approach. 2021.

[10] ESA. Space debris by the numbers. https://www.esa.int/Space_Safety/Space_Debris/Space_debris_by_the_numbers, . Accessed: 24th October 2023.

[11] ESA. Mitigating space debris generation. https://www.esa.int/Space_Safety/Space_Debris/Mitigating_space_debris_generation, . Accessed: 22nd October 2023.

[12] ESA. About space debris. https://www.esa.int/Space_Safety/Space_Debris/About_space_debris, . Accessed: 24th October 2023.

[13] P. Farinella and A. Cordelli. The proliferation of orbiting fragments: A simple mathematical model. *Science and Global Security*, 2, 1991. ISSN 15477800. doi: 10.1080/08929889108426373.

[14] S. Frey. *Evolution and hazard analysis of orbital fragmentation continua*. PhD thesis, Politecnico di Milano, 2020.

[15] S. Frey and C. Colombo. Transformation of satellite breakup distribution for probabilistic orbital collision hazard analysis. *Journal of Guidance, Control, and Dynamics*, 44, 2021. ISSN 15333884. doi: 10.2514/1.G004939.

[16] S. Frey, C. Colombo, and S. Lemmens. Application of density-based propagation to fragment clouds using the starling suite. *First International Orbital Debris Conference*, 2019.

[17] S. Frey, C. Colombo, and S. Lemmens. Extension of the king-hele orbit contraction method for accurate, semi-analytical propagation of non-circular orbits. *Advances in Space Research*, 64, 2019. doi: 10.1016/j.asr.2019.03.016.

[18] L. Giudici, J. L. Gonzalo, and C. Colombo. Density-based in-orbit collision risk model extension to any impact geometry, 2023. arXiv:2309.03562.

[19] L. Giudici, M. Trisolini, and C. Colombo. Probabilistic multi-dimensional debris cloud propagation subject to non-linear dynamics. *Advances in Space Research*, 72, 2023. ISSN 18791948. doi: 10.1016/j.asr.2023.04.030.

[20] N. N. Gor'kavyi, L. M. Ozernoy, and J. C. Mather. A new approach to dynamical evolution of interplanetary dust. *The Astrophysical Journal*, 474, 1997. ISSN 0004-637X. doi: 10.1086/303440.

[21] W. B. Heard. Dispersion of ensembles of non-interacting particles. *Astrophysics and Space Science*, pages 43,63–82, 1976.

[22] R. Jehn. Dispersion of debris clouds from in-orbit fragmentation events. *ESA Journal*, 15, 1991.

[23] A. B. Jenkin. Probability of collision during early evolution of debris clouds. *Acta Astronautica*, 38:525–538, 1996.

[24] F. John. *Partial Differential Equations, Applied Mathematical Sciences*. Springer, 4th edition, 1991. ISBN 0.387-90609.

[25] N. L. Johnson, P. H. Krisko, J. C. Liou, and P. D. Anz-Meador. Nasa's new breakup model of evolve 4.0. *Advances in Space Research*, 28, 2001. ISSN 02731177. doi: 10.1016/S0273-1177(01)00423-9.

[26] N. L. Johnson, E. Stansbery, D. O. Whitlock, K. J. Abercromby, and D. Shoots. History of on-orbit satellite fragmentations 14th edition. *Houston: NASA*, 2008.

[27] D. J. Kessler. Derivation of the collision probability between orbiting objects: the lifetimes of jupiter's outer moons. *Icarus*, 48, 1981. ISSN 10902643. doi: 10.1016/0019-1035(81)90151-2.

[28] D. J. Kessler and B. G. Cour-Palais. Collision frequency of artificial satellites: The creation of a debris belt. *J Geophys Res*, 83, 1978. ISSN 0148-0227. doi: 10.1029/JA083iA06p02637.

[29] D. J. Kessler, N. L. Johnson, J. C. Liou, and M. Matney. The kessler syndrome: Implications to future space operations. *Advances in the Astronautical Sciences*, 137, 2010. ISSN 00653438.

[30] D. G. King-Hele. *Theory of Satellite Orbits in an Atmosphere*. Butterworths, 1964.

[31] F. Letizia. *Space debris cloud evolution in Low Earth Orbit*. PhD thesis, University of Southampton, Faculty of Engineering and the Environment, 2016.

[32] F. Letizia. Extension of the density approach for debris cloud propagation. *Journal of Guidance, Control, and Dynamics*, 41:2650–2656, 2018. ISSN 15333884. doi: 10.2514/1.G003675.

[33] F. Letizia, C. Colombo, and H. G. Lewis. Continuity equation approach for the analysis of the collision risk due to space debris clouds generated by a fragmentation event. *Proceedings of the International Astronautical Congress, IAC*, 3, 2014.

[34] F. Letizia, C. Colombo, and H. G. Lewis. Analytical model for the propagation of small-debris-object clouds after fragmentations. *Journal of Guidance, Control, and Dynamics*, 38, 2015. ISSN 15333884. doi: 10.2514/1.G000695.

[35] F. Letizia, H. G. Lewis, and C. Colombo. 2d continuity equation method for space debris cloud collision analysis. In *25th AAS/AIAA Space Flight Mechanics Meeting*, 2015.

[36] F. Letizia, C. Colombo, and H. G. Lewis. Collision probability due to space debris clouds through a continuum approach. *Journal of Guidance, Control, and Dynamics*, 39, 2016. ISSN 15333884. doi: 10.2514/1.G001382.

[37] F. Letizia, C. Colombo, and H. G. Lewis. Multidimensional extension of the continuity equation method for debris clouds evolution. *Advances in Space Research*, 57, 2016. ISSN 18791948. doi: 10.1016/j.asr.2015.11.035.

[38] F. Letizia, C. Colombo, H. G. Lewis, and H. Krag. Assessment of breakup severity on operational satellites. *Advances in Space Research*, 58, 2016. ISSN 18791948. doi: 10.1016/j.asr.2016.05.036.

[39] F. Letizia, C. Colombo, H. G. Lewis, and H. Krag. Extending the ecob space debris index with fragmentation risk estimation. *7th European Conference on Space Debris, Darmstadt, Germany*, 2017.

[40] F. Letizia, C. Colombo, H. G. Lewis, and H. Krag. Development of a debris index. *Astrophysics and Space Science Proceedings*, 52, 2018. ISSN 15706605. doi: 10.1007/978-3-319-69956-1_12.

[41] F. Letizia, S. Lemmens, B. B. Virgili, and H. Krag. Application of a debris index for global evaluation of mitigation strategies. *Acta Astronautica*, 161, 2019. ISSN 00945765. doi: 10.1016/j.actaastro.2019.05.003.

[42] H. G. Lewis, S. G. George, B. S. Schwarz, and H. Stokes. Space debris environment impact rating system. *6th European Conference on Space Debris*, 2013:22–25, 2013.

[43] J. C. Liou. Collision activities in the future orbital debris environment. *Advances in Space Research*, 38, 2006. ISSN 02731177. doi: 10.1016/j.asr.2005.06.021.

[44] J. C. Liou, D. T. Hall, P. H. Krisko, and J. N. Opiela. Legend - a three-dimensional leo-to-geo debris evolutionary model. In *Advances in Space Research*, volume 34, 2004. doi: 10.1016/j.asr.2003.02.027.

[45] J. C. McDowell. The low earth orbit satellite population and impacts of the spacex starlink constellation. *The Astrophysical Journal*, 892, 2020. ISSN 20418213. doi: 10.3847/2041-8213/ab8016.

[46] C. McInnes. An analytical model for the catastrophic production of orbital debris. *ESA journal 17(4)*, pages 293–305, 1993.

[47] C. R. McInnes. Simple analytic model of the long-term evolution of nanosatellite constellations. *Journal of Guidance, Control, and Dynamics*, 23, 2000. ISSN 07315090. doi: 10.2514/2.4527.

[48] D. McKnight. A phased approach to collision hazard analysis. *Advances in Space Research*, 10, 1990. doi: 10.1016/0273-1177(90)90374-9.

[49] F. Mclean, S. Lemmens, Q. Funke, and V. Braun. Discos 3: An improved data model for esa's database and information system characterising objects in space. *7th European Conference on Space Debris, Darmstadt*, 7, 2017.

[50] A. Muciaccia, M. Trisolini, L. Giudici, C. Colombo, B. D. Campo, and F. Letizia. Environmental impact of large constellations through a debris index analysis. *Proceedings of the International Astronautical Congress, IAC*, 2022-September, 2022. ISSN 00741795.

[51] A. Muciaccia, L. Giudici, M. Trisolini, C. Colombo, B. D. C. Lopez, F. Letizia, and S. Lemmens. Space environment investigation using a space debris index, 2023.

[52] E. S. D. Office. Esa's annual space environment report, 4 2022.

[53] E. S. D. Office. Esa's annual space environment report. Technical report, ESA ESOC, 2023.

[54] C. Pardini and L. Anselmo. Evolution of the debris cloud generated by the fengyun-1c fragmentation event. *Proceedings of the 20th ISSFD*, 2007.

[55] C. Pardini and L. Anselmo. Physical properties and long-term evolution of the debris clouds produced by two catastrophic collisions in earth orbit. *Advances in Space Research*, 48:557–569, 8 2011. ISSN 02731177. doi: 10.1016/j.asr.2011.04.006.

[56] C. Pardini and L. Anselmo. The short-term effects of the cosmos 1408 fragmentation on neighboring inhabited space stations and large constellations. *Acta Astronautica*, 210:465–473, 9 2023. ISSN 00945765. doi: 10.1016/j.actaastro.2023.02.043.

[57] D. S. F. Portree and J. P. Loftus. Orbital debris: A chronology. *NASA*, TP-1999-2, 1999.

[58] S. M. Ross. A first course in probability 8th ed. solutions manual. *The American Statistician*, 2010. ISSN 0003-1305.

[59] A. Rossi, A. Cordelli, P. Farinella, and L. Anselmo. Collisional evolution of the earth's orbital debris cloud. *Journal of Geophysical Research*, 99, 1994. ISSN 01480227. doi: 10.1029/94je02320.

[60] A. Rossi, L. Anselmo, A. Cordelli, P. Farinella, and C. Pardini. Modelling the evolution of the space debris population. *Planetary and Space Science*, 46, 1998. ISSN 00320633. doi: 10.1016/s0032-0633(98)00070-1.

[61] A. Rossi, L. Anselmo, C. Pardini, R. Jehn, and G. B. Valsecchi. The new space debris mitigation (sdm 4.0) long term evolution code. In *European Space Agency, (Special Publication) ESA SP*, volume 672 SP, 2009.

[62] A. Rossi, G. B. Valsecchi, and E. M. Alessi. The criticality of spacecraft index. *Advances in Space Research*, 56, 2015. ISSN 18791948. doi: 10.1016/j.asr.2015.02.027.

[63] G. L. Somma, H. G. Lewis, and C. Colombo. Adaptive remediation of the space debris environment using feedback control. In *Proceedings of the International Astronautical Congress, IAC*, 2016.

[64] G. L. Somma, C. Colombo, and H. G. Lewis. A statistical leo model to investigate adaptable debris control strategies. In *7th European Conference on Space Debris*, 2017. doi: 10.13140/2.1.

[65] G. L. Somma, H. G. Lewis, and C. Colombo. Sensitivity analysis of launch activities in low earth orbit. *Acta Astronautica*, 158, 2019. ISSN 00945765. doi: 10.1016/j.actaastro.2018.05.043.

[66] S. Y. Su and D. J. Kessler. Contribution of explosion and future collision fragments to the orbital debris environment. *Advances in Space Research*, 5, 1985. ISSN 02731177. doi: 10.1016/0273-1177(85)90384-9.

[67] D. L. Talent. Analytic model for orbital debris environmental management. *Journal of Spacecraft and Rockets*, 29, 1992. ISSN 00224650. doi: 10.2514/3.25493.

[68] M. Trisolini and C. Colombo. A density-based approach to the propagation of re-entry uncertainties. *Advances in the Astronautical Sciences*, 168, 2019. ISSN 00653438.

[69] D. A. Vallado. *Fundamentals of astrodynamics and applications*. Springer, 4th edition, 2013. ISBN 978-1881883180.

[70] B. B. Virgili. Delta (debris environment long-term analysis). In *Proceedings of the 6th International Conference on Astrodynamics Tools and Techniques (ICATT)*, 2016.

[71] R. Walker, C. E. Martin, P. H. Stokes, J. E. Wilkinson, and H. Klinkrad. Analysis of

the effectiveness of space debris mitigation measures using the delta model. *Advances in Space Research*, 28, 2001. doi: 10.1016/S0273-1177(01)00445-8.

[72] E. J. Öpik. Collision probabilities with the planets and the distribution of interplanetary matter. In *Proceedings of the Royal Irish Academy. Section A: Mathematical and Physical Sciences*, volume 54, 1951.

A | Appendix A

In this appendix, the distributions in A/M and velocity variation employed in the implementation of the NASA Standard Breakup Model are reported. The distribution in A/M is dependent on the type of object involved in the breakup (rocket body or spacecraft) and the characteristic size L_c.

When a spacecraft is involved in the breakup and fragments are larger than 11 cm, the distribution function is given by:

$$D_{A/M}(\lambda_c, \chi) = \alpha(\lambda_c)\mathcal{N}(\mu_1(\lambda_c), \sigma_1(\lambda_c), \chi) + (1 - \alpha(\lambda_c))\mathcal{N}(\mu_2(\lambda_c), \sigma_2(\lambda_c), \chi) \tag{A.1}$$

where χ is the variable in the distribution and $\mathcal{N}$ is the normal distribution function and

$$\begin{aligned} &\lambda_c = \log_{10}(L_c), \\ &\chi = \log_{10}(A/M), \\ &\mathcal{N}(\mu, \sigma, \chi) = \frac{1}{\sigma\sqrt{2\pi}} \exp\left(-\frac{(\chi - \mu)^2}{2\sigma^2}\right). \end{aligned} \tag{A.2}$$

The variables in Equation A.1 are piecewise functions of λ_c:

$$\alpha(\lambda_c) = \begin{cases} 0 & \lambda_c \leq -1.95 \\ 0.3 + 0.4(\lambda_c + 1.2) & -1.95 < \lambda_c < 0.55 \\ 1 & \lambda_c \geq 0.55 \end{cases}$$

$$\mu_1(\lambda_c) = \begin{cases} -0.6 & \lambda_c \leq -1.1 \\ -0.6 - 0.318(\lambda_c + 1.1) & -1.1 < \lambda_c < 0 \\ -0.95 & \lambda_c \geq 0 \end{cases}$$

$$\sigma_1(\lambda_c) = \begin{cases} 0.1 & \lambda_c \leq -1.3 \\ 0.1 + 0.2(\lambda_c + 1.3) & -1.3 < \lambda_c < -0.3 \\ 0.3 & \lambda_c \geq -0.3 \end{cases}$$

$$\mu_2(\lambda_c) = \begin{cases} -1.2 & \lambda_c \leq -0.7 \\ -1.2 - 1.333(\lambda_c + 0.7) & -0.7 < \lambda_c < -0.1 \\ -2.0 & \lambda_c \geq -0.1 \end{cases}$$

$$\sigma_2(\lambda_c) = \begin{cases} -0.5 & \lambda_c \leq -0.5 \\ 0.5 - (\lambda_c + 0.5) & -0.5 < \lambda_c < -0.3 \\ 0.3 & \lambda_c \geq -0.3 \end{cases}$$

For rocket bodies, the A/M distribution follows a similar behaviour. In particular, for fragments larger than 11 cm, the distribution function is given by:

$$D_{A/M}(\lambda_c, \chi) = \alpha(\lambda_c)\mathcal{N}(\mu_1(\lambda_c), \sigma_1(\lambda_c), \chi) + (1 - \alpha(\lambda_c))\mathcal{N}(\mu_2(\lambda_c), \sigma_2(\lambda_c), \chi) \tag{A.3}$$

with

$$\alpha(\lambda_c) = \begin{cases} 1 & \lambda_c \leq -1.4 \\ 1 - 0.3571(\lambda_c + 1.4) & -1.4 < \lambda_c < 0 \\ 0.5 & \lambda_c \geq 0 \end{cases}$$

$$\mu_1(\lambda_c) = \begin{cases} -0.45 & \lambda_c \leq -0.5 \\ -0.45 - 0.9(\lambda_c + 0.5) & -0.5 < \lambda_c < 0 \\ 0 - 0.9 & \lambda_c \geq 0 \end{cases}$$

$$\sigma_1(\lambda_c) = 0.55$$

$$\mu_2(\lambda_c) = -0.9$$

$$\sigma_2(\lambda_c) = \begin{cases} 0.28 & \lambda_c \leq -1.0 \\ 0.28 - 0.1636(\lambda_c + 1) & -1.0 < \lambda_c < 0.1 \\ 0.1 & \lambda_c \geq 0.1 \end{cases}$$

When fragments are smaller than 8 cm, the distribution function becomes:

$$D_{A/M}(\lambda_c, \chi) = \mathcal{N}(\mu(\lambda_c), \sigma(\lambda_c), \chi) \tag{A.4}$$

where

$$\mu(\lambda_c) = \begin{cases} -0.3 & \lambda_c \leq -1.75 \\ -0.3 - 1.4(\lambda_c + 1.75) & -1.75 < \lambda_c < -1.25 \\ -1.0 & \lambda_c \geq -1.25 \end{cases}$$

$$\sigma(\lambda_c) = \begin{cases} 0.2 & \lambda_c \leq -3.5 \\ 0.2 + 0.1333(\lambda_c + 3.5) & \lambda_c > -3.5 \end{cases}$$

A bridge function is used for the fragments between 8 cm and 11 cm:

$$B(\lambda_c) = 10(\lambda_c + 1.105) \tag{A.5}$$

The model computes the value of the bridge function and then a random number. If the number is greater than the value of the bridge function, the fragment is treated as a big object and vice versa.

As for the velocity variation distribution, it depends on the area-to-mass ratio and on the type of fragmentation. For explosions, the distribution is given by:

$$D_{\Delta v}(\chi, \xi) = \mathcal{N}(\mu(\chi), \sigma(\chi), \xi) \tag{A.6}$$

where in this case:

$$\begin{aligned} \chi &= \log_{10}(A/M), \\ \xi &= \log_{10}(\Delta v), \\ \mu(\chi) &= 0.2\chi + 1.85, \\ \sigma(\chi) &= 0.4. \end{aligned} \tag{A.7}$$

Lastly, the velocity variation distribution for collisions is given by the same expression as Equation A.7, but with different mean and standard deviation:

$$\begin{aligned} \mu(\chi) &= 0.9\chi + 2.9, \\ \sigma(\chi) &= 0.4. \end{aligned}$$

B | Appendix B

The method of characteristics allows to obtain the solution of Partial Differential Equation (PDE) by solving systems of Ordinary Differential Equations (ODE) along specific curves called *characteristics*. The primary principles of the method of characteristics are recalled here from [24], then its application to the continuity equation as in [31] is detailed.

B.1. General method

We start by considering a simple case of the general first-order equation, that is a quasi-linear equation in the independent variables x and y:

$$a(x, y, u)u_x + b(x, y, u)u_y = c(x, y, u) \tag{B.1}$$

where the solution $u(x, y)$ is represented as a surface, called *integral surface,* $z = u(x, y)$ in the xyz-space. The vectors $a(x, y, z), b(x, y, z)$ and $c(x, y, z)$ are distinguished by their *characteristic directions*. The vector $(u_x, u_y, -1)$ represents the normal to the integral surface, therefore Eq. B.1 is equivalent to the condition that the normal of the integral surface at any point is perpendicular to the direction of the vector (a, b, c) corresponding to that point. This can be translated in the condition that at each point (x, y):

$$(a(x, y), b(x, y)c(x, y)) \cdot (u_x(x, y), u_y(x, y), -1) = 0. \tag{B.2}$$

that is, the vector (a, b, c) is tangent to the integral surface z at any point. We can associate a family of *characteristic curves* to the field of characteristic directions such that at any point the characteristic curves are tangent to that direction field and along each curve the following relation holds:

$$\frac{dx}{a(x, y)} = \frac{dy}{b(x, y)} = \frac{dz}{c(x, y)}. \tag{B.3}$$

The previous condition can be written in the form of a system of ODE by parametrising the curve with respect to a parameter s:

$$\begin{aligned}\frac{dx}{ds} &= a(x,y),\\ \frac{dy}{ds} &= b(x,y),\\ \frac{dz}{ds} &= c(x,y).\end{aligned} \tag{B.4}$$

The integral surface $z = u(x,y)$, solution of Eq. B.1, is the union of the characteristic curves found by solving the system B.4, which is known as the set of characteristic equations for Eq. B.1. Introducing these characteristic equations allows to reduce a PDE to a system of ODE.

B.2. Application

Eq. 2.40 is equivalent to the PDE in Eq. B.1, hence the corresponding system of ODE obtained with the method of characteristics is:

$$\frac{dt}{ds} = 1 \tag{B.5}$$

$$\frac{dr}{ds} = v_r \tag{B.6}$$

$$\frac{dn}{ds} = -\left[\frac{2}{r}v_r + v_r'\right] n(r,t) \tag{B.7}$$

Eq. B.5 clarifies that the parameter s corresponds to the time t, therefore Eq. B.6 can be rewritten:

$$\frac{dr}{dt} = v_r = -\epsilon\sqrt{r}\exp\left(-\frac{r-R_h}{H}\right) \tag{B.8}$$

where the expression for v_r is the one of Eq. 2.38. To obtain a full analytical solution, it is necessary to introduce an approximation for the radial distance: $\sqrt{r} \approx \sqrt{R_h}$, leading to

$$\frac{dr}{dt} \approx -\epsilon\sqrt{R_h}\exp\left(-\frac{r-R_h}{H}\right). \tag{B.9}$$

and its corresponding solution:

$$\exp\left(-\frac{r-R_h}{H}\right) + \epsilon\frac{\sqrt{R_h}}{H}t = \tilde{C}. \tag{B.10}$$

Putting together Eqs. B.6 and B.7 we obtain:

$$\left[\frac{2}{r}v_r + v_r'\right]\frac{dr}{v_r} = -\frac{dn}{n} \tag{B.11}$$

Integrating the left-hand side of the equation:

$$\int \frac{1}{v_r}\left[\frac{2}{r}v_r + v_r'\right]\,dr = \log\left(\frac{1}{r^2 v_r}\right) + c \tag{B.12}$$

Therefore one can obtain the density evolution defining the function $\Psi[G(r,t)]$ which is an arbitrary function of the characteristics derived from the initial distribution $n(r,0)$ as in Eq. 2.44. The solution of the continuity equation then becomes:

$$n(r,t) = \frac{\Psi[G(r,t)]}{r^2 v_r(r)} = \frac{\Psi\left\{\exp[\frac{r-R_h}{H}] + (\epsilon\sqrt{R_h}/H)t\right\}}{-\epsilon r^{5/2}\exp[-\frac{r-R_h}{H}]}. \tag{B.13}$$

List of Figures

1.1 Evolution of the number of objects in geocentric orbit [53]. 2
1.2 Cumulative number of catastrophic collisions in the simulated long-term evolution of the environment [53]. 4

2.1 Block diagram of the continuum approach. 15
2.2 Phases of debris cloud evolution for a collision 19
2.3 Error on the density profile for ten runs of the NASA Standard Breakup Model after 1000 days of propagation. 29
2.4 Error on the fragment number for ten runs of the NASA Standard Breakup Model after 1000 days of propagation. 29
2.5 Profile error and fragment number error for logspaced bins from 1 to 15 bins. 31
2.6 Profile error and fragment number error for bins with the same number of fragments, from 1 to 15 bins. 31
2.7 Fragment number error for bins with the same number of fragments, from 1 to 15 with respect to the altitude of fragmentation. 32
2.8 Distribution of area-to-mass ratio and velocity variation of the fragments generated in the Cosmos 1867 breakup. 34
2.9 Gabbard diagram right after the fragmentation: apocentre and pericentre distribution as a function of the orbital period. 34
2.10 Alternative representation of the Gabbard diagram right after the fragmentation (a) and at the moment of band formation (b). 35
2.11 Spatial density function of the debris cloud at band formation. 36
2.12 Evolution of the spatial density of the debris cloud in time starting from the band formation. 36
2.13 Evolution of the peak altitude for each area-to-mass ratio bin. 37
2.14 Spatial density function of the debris cloud at band formation. 38

3.1 Building blocks of the continuum approach with the collision probability computation. 41

3.2 Spherical triangles due to the intersection between target and fragments orbit [18]. 44
3.3 Impact rate in time. 46
3.4 Collision probability in time. 46
3.5 Impact rate with respect to spacecraft 1 position and time. 47

4.1 LEO region representative targets in semi-major axis and inclination grid in 2017 (a), 2023 (b) and 2023 including Starlink (c). 51
4.2 Analysis of the lifetime of a debris cloud with respect to its altitude (a) and variation of the time step with altitude (b). 54
4.3 Analysis on the evolution of fragments in orbit in time (a) and remaining fragments after the lifetime of the cloud (b) at various altitudes. 55
4.4 Effect maps of catastrophic collisions with targets of 2017 (a), 2023 (b) and 2023 with Starlink constellation (c), with a fixed Δt. Fragments lower size 1 cm. 56
4.5 Effect map obtained with the THEMIS software for catastrophic collisions with 2023 targets without constellations, from [7]. 57
4.6 Effect maps of catastrophic collisions with targets of 2017 (a), 2023 (b) and 2023 with Starlink constellation (c), with a variable Δt. Fragments lower size 1 cm. 59
4.7 Details of the effect maps at low altitudes when considering a fixed Δt (a) and a variable Δt (b). 60
4.8 Effect maps of non-catastrophic collisions with targets of 2017 (a), 2023 (b) and 2023 with Starlink constellation (c), with a fixed Δt. Fragments lower size 1 mm. 61
4.9 Effect maps of non-catastrophic collisions with targets of 2017 (a), 2023 (b) and 2023 with Starlink constellation (c), with a variable Δt. Fragments lower size 1 mm. 62
4.10 Effect maps with targets of 2017 (a), 2023 (b) and 2023 with Starlink constellation (c), with a fixed Δt for rocket-body explosions. Fragments lower size 5 mm. 63
4.11 Effect maps with targets of 2017 (a), 2023 (b) and 2023 with Starlink constellation (c), with a variable Δt for rocket-body explosions. Fragments are considered down to 5 mm size. 64

List of Tables

2.1 Cosmos 1867 breakup characteristics. 28
2.2 Average errors for the three bin definitions 30
2.3 Breakup characteristics 33
2.4 Average computational times for the analytic and numerical methods. . . . 38

3.1 Characteristics of the targets. 45

List of Symbols

Variable	Description	SI unit
A	Cross-sectional area	m^2
a	Semi-major axis	km
A/M	Area-to-mass ratio	m^2/kg
a_d	Drag acceleration	m/s^2
β	Latitude	rad
c_D	Drag coefficient	$-$
e	Eccentricity	$-$
e_c	Effect of collisions	[-]
e_e	Effect of explosions	[-]
E	Eccentric anomaly	rad
ϵ	Orbital energy	km^2/s^2
$\mathbf{f}$	Vector field	$-$
$\tilde{E}_p$	Specific impact energy	J/g
f	True anomaly	rad
H	Scale height for atmospheric model	km
h	Altitude	km
i	Inclination	rad
I_k	Modified Bessel function of the first kind of order k	$-$
J_2	Second zonal harmonic coefficient of the Earth's gravitational potential	$-$
λ	Longitude	rad
L_c	Characteristic length	m
M	Mass	kg
$\overline{M}$	Mean anomaly	rad
M_p	Projectile mass	kg
μ	Mean	$-$
μ_E	the Earth's gravitational parameter	km^3/s^2
N	Spatial density function	$1/km^3$

Variable	Description	SI unit
$\dot{\eta}$	Impact rate	$year^{-1}$
N_f	Number of fragments	$-$
ω	Argument of pericentre	rad
Ω	Right ascension of the ascending node	rad
p	Semi-latus rectum	km
p_c	Cumulative collision probability	$-$
r	Radial distance from the centre of the Earth	km
ρ	Atmospheric density	kg/m^3
R_E	The Earth's mean radius	km
R_h	Reference altitude for the atmospheric model	km
t	Time	s
T_B	Band formation time	s
T_Ω	Nodal dispersion in time	s
T_ω	Apsidal dispersion in time	s
τ_L	Lifetime of a fragment	s
u	Argument of latitude	rad
v_{rel}	Relative impact velocity	km/s

Acronyms

A/M area-to-mass ratio.

ADR Active Debris Removal.

CiELO debris Cloud Evolution in Low (Earth) Orbit.

CSI Criticality of Spacecraft Index.

DELTA Debris Environment Long Term Analysis.

DISCOS Database and Information System Characterising Objects in Space.

ECOB Environmental Consequences of Orbital Breakups.

ESA European Space Agency.

GEO Geostationary Orbit.

GMM Gaussian Mixture Model.

IADC Inter-Agency Space Debris Coordination Committee.

LEGEND LEO-to-GEO Environment Debris.

LEO Low Earth Orbit.

MEO Medium Earth Orbit.

MRO Mission Related Objects.

NASA National Aeronautics and Space Administration.

ODE Ordinary Differential Equations.

PDE Partial Differential Equation.

PIB "particles-in-a-box".

PMD Post Mission Disposal.

RAAN Right Ascension of the Ascending Node.

SDM Space Debris Mitigation.

SRP Solar Radiation Pressure.

THEMIS Track the Health of the Environment and Missions in Space.

Acknowledgements

In this last Chapter, I want to thank some people who have played a fundamental role in my academic years.
First, I would like to thank Professor Camilla Colombo for giving me the opportunity of working on such an interesting topic and for her supervision. I also wish to express my gratitude to my co-supervisors, Lorenzo Giudici and Martina Rusconi, for their precious advice and guidance and for all the meetings of the past months, which have been crucial for the completion of this thesis.

A special thanks is dedicated to my family, for the constant support they have given me throughout these five years and for enabling me to succeed in this path. I wouldn't be where I am today without the endless support and patience they have shown me, both in bad and good times.

Lastly, I want to thank my friends: the ones I met the very first year of university, the ones I have shared the last two years with and the friends I have met abroad, for everything we have shared. Without them, these past years full of laughter, but also tough moments, would not have been the same.